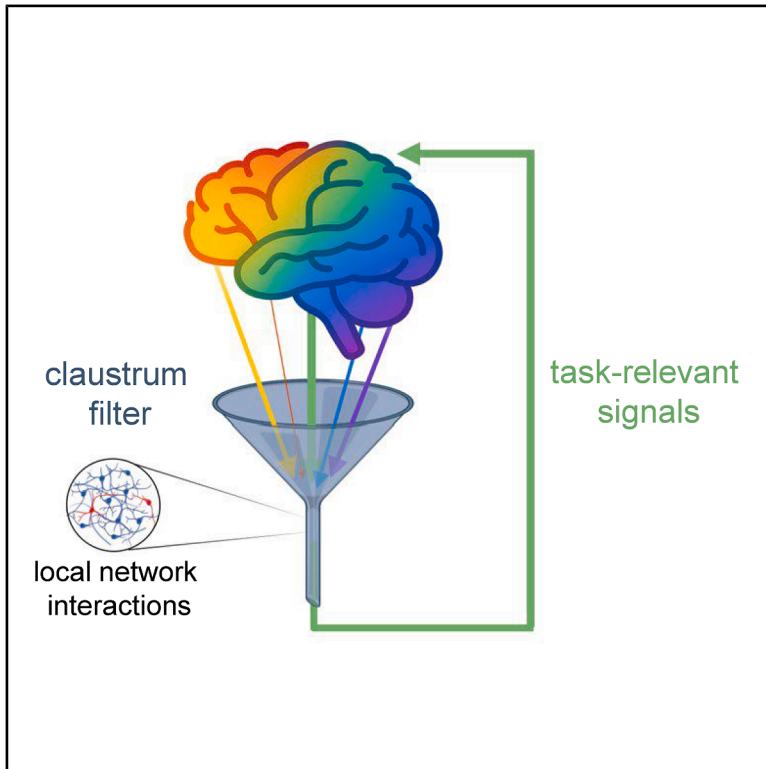


Mapping the functional connectome of the claustrum: Noise filtering via local inhibitory circuits

Graphical abstract



Authors

Martin Graf, Sadra Sadeh,
George J. Augustine

Correspondence

george_augustine@tll.org.sg

In brief

Graf et al. optogenetically mapped 24 inhibitory circuits formed between interneurons and postsynaptic targets within the claustrum. A computational model predicts that the spatial structure of local circuits filters claustral input, and experimental tests confirm model predictions. Claustrum filtering precisely transforms excitatory input into output to cortical and subcortical targets.

Highlights

- Claustrum interneurons form local inhibitory and disinhibitory circuit motifs
- Computational modeling predicts that these circuits serve as spatial and amplitude filters
- Experimental tests confirmed the hypothesized network computations
- The claustrum may contribute to cognitive function by filtering task-relevant signals



Article

Mapping the functional connectome of the claustrum: Noise filtering via local inhibitory circuits

Martin Graf,^{1,2,3} Sadra Sadeh,^{4,5} and George J. Augustine^{1,2,6,*}¹Temasek Life Sciences Laboratory, Singapore, Singapore²Neuroscience & Mental Health Program, Lee Kong Chian School of Medicine, Nanyang Technological University, Singapore, Singapore³Department of Neuroscience and Mental Health, Boehringer Ingelheim Pharma GmbH & Co. KG, Birkendorfer Str. 65, Biberach Riß 88397, Germany⁴Centre for Developmental Neurobiology, King's College London, London, UK⁵The Francis Crick Institute, London, UK⁶Lead contact*Correspondence: george_augustine@tll.org.sg<https://doi.org/10.1016/j.celrep.2025.116821>

SUMMARY

We optogenetically mapped the function and spatial organization of inhibitory circuits formed by interneurons (INs) within the claustrum, a highly interconnected but poorly understood brain region. INs expressing parvalbumin or somatostatin attenuate claustrum output by inhibiting projection neurons (PNs), while INs expressing vasoactive intestinal peptide promote claustrum output by disinhibiting PNs. The spatial organization and degree of convergence differ for each interneuronal circuit. A computational model incorporating measured circuit properties predicts that differential inhibition of PNs by INs toggles claustrum output between cortical and subcortical brain regions and that the spatial organization of IN circuits nonlinearly filters claustrum output according to the strength and spatial distribution of excitatory input. Experimental measurements show that the claustrum spatially filters cortical input as predicted by the model. We conclude that the organization of its inhibitory circuits allows the claustrum to serve as a filter that improves the signal-to-noise ratio of signals transmitted to its downstream targets.

INTRODUCTION

The claustrum is a thin subcortical structure that has been implicated in a wide variety of behaviors, including attention,^{1–3} task-related motor responses,⁴ impulsivity,^{4,5} reward learning,⁶ aversive associative learning,⁷ anxiety,⁸ sleep,^{9–12} and pain.¹³ While such studies address the question of what the claustrum does, we still lack even a rudimentary understanding of how it works. These diverse functions of the claustrum must be subserved by its local circuitry, as well as by its widespread connections with other cortical and subcortical structures.^{14–16} Cortical inputs are topographically organized to target specific claustral subregions¹⁷; these inputs excite claustral projection neurons (PNs), with PNs receiving less input from sensory areas than frontal areas.^{18–20} Claustral PNs can integrate inputs from multiple cortical areas^{16,18} and receive local input, chiefly from interneurons (INs) that inhibit and provide feedback to PNs.^{4,20,21} These INs also receive excitatory cortical input.^{18,21} Because inhibition controls network output,^{21,22} a better understanding of local IN circuitry is required to decode the functions of the claustrum.

Here, we have combined optogenetic circuit mapping^{23–25} with computational modeling to define the inhibitory connectome of the claustrum. We identified circuit motifs that are formed by distinct subtypes of INs and have created a model of these

circuits to deduce the contributions of each IN subtype to claustral computation. Further, we validated model predictions with experimental measurements of claustral transformation of cortical input. Together, our results indicate that claustral INs are wired to serve as a filter that nonlinearly reduces noise according to the strength and location of cortical inputs. Additionally, local IN circuitry enables the claustrum to dynamically toggle its output between cortical and subcortical targets. Our findings greatly expand knowledge of claustral circuit organization and provide a “bottom-up” explanation for how the claustrum can contribute to diverse behaviors by serving as a filter.

RESULTS

We characterized inhibitory circuits between presynaptic INs and their postsynaptic targets. Channelrhodopsin-2 (ChR2) was transgenically expressed in the 3 major subtypes of claustral INs,²⁶ under the control of their defining promoters: parvalbumin (PV), somatostatin (SST), or vasoactive-intestinal peptide (VIP). Together, these 3 subtypes represent more than 90% of all claustral INs.²⁶ In coronal brain slices from these transgenic mice, whole-cell patch clamp recordings revealed that widefield photostimulation (480 nm, 1.2 or 500 ms duration; [Figure 1A](#)) broadly activated ChR2-expressing INs within the microscope



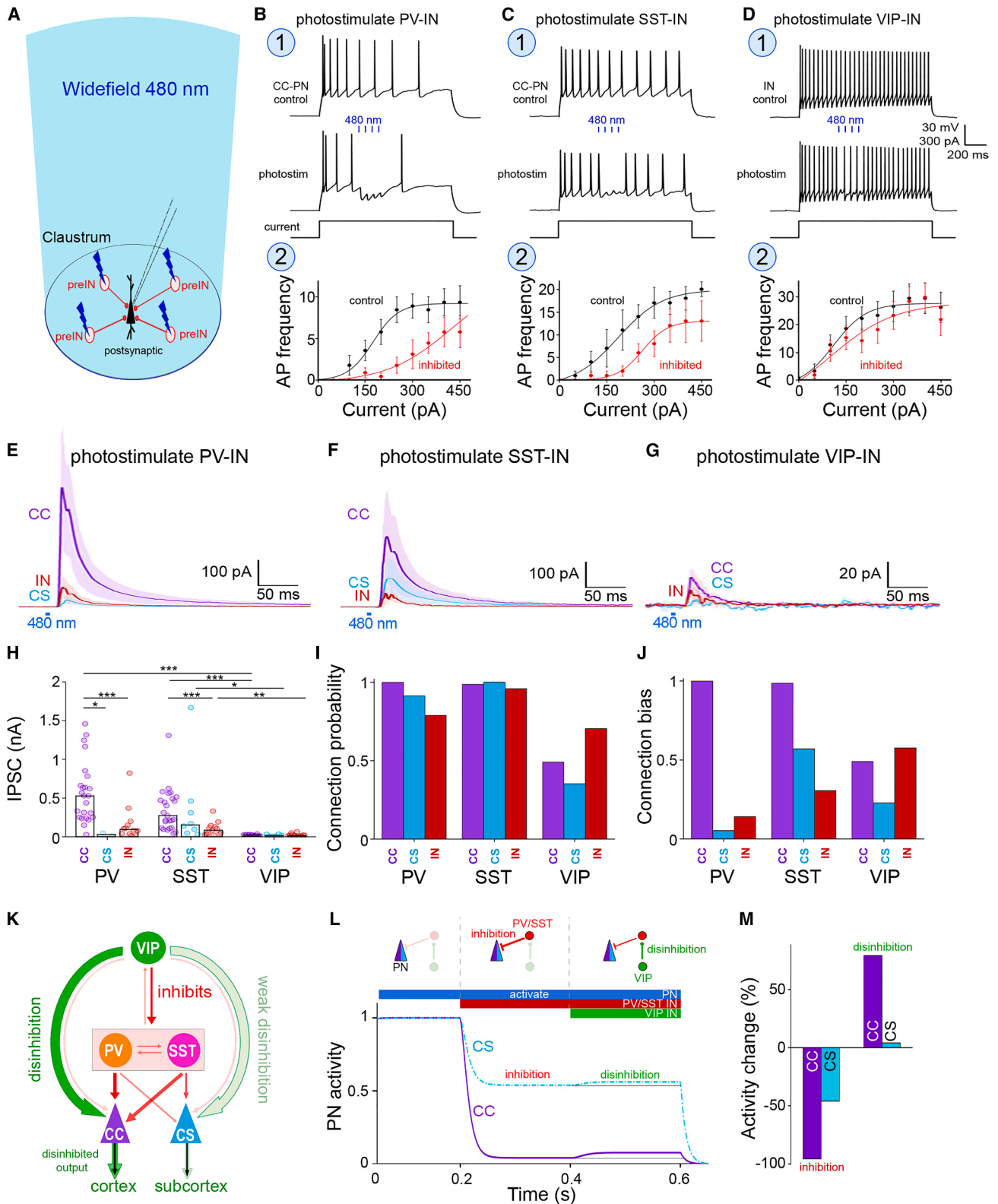


Figure 1. Connection-specific inhibition evoked by widefield photostimulation of INs

(A) Detecting responses to widefield photostimulation: a postsynaptic neuron (black) was patched, while a 480-nm light flash (blue shading) activated ChR2-expressing INs (red) within the light beam to evoke IPSCs in the postsynaptic neuron.

(legend continued on next page)

field and generated inhibitory postsynaptic potentials (IPSPs) that reduced action potential (AP) firing in their postsynaptic targets (Figures 1B1–1D1). As a result of such inhibition, activation of each subtype of presynaptic INs caused a rightward shift in the relationship between depolarizing current input and postsynaptic AP output (Figures 1B2–1D2).

These inhibitory responses varied according to both presynaptic and postsynaptic neuron identity. Based on a previous classification scheme,²⁶ five postsynaptic PN subtypes and the three postsynaptic IN subtypes could be distinguished by their intrinsic electrical properties (Figure S1). This scheme is based on a large number of electrical properties that correctly distinguish INs from PNs with 97% accuracy, distinguish between PN subtypes with 89% accuracy, and identify IN subtypes with 93% accuracy, as independently assessed by marker gene expression and retrograde labeling.²⁶ We have analyzed the entire matrix of 24 inhibitory connections (3 presynaptic IN subtypes and 8 postsynaptic neuron subtypes). For simplicity, postsynaptic targets were parsed into three functional groups: all cortically projecting PNs (PN2–PN5) were grouped as claustrum-cortical projection neurons (CC-PN), subcortically projecting PN1 was named CS-PN, while PV-INs, SST-INs, and VIP-INs were pooled as INs (Figure S1). While we focus on the 9 connections between PV-INs, SST-INs, and VIP-INs and their postsynaptic CC-PNs, CS-PNs, and INs, the comprehensive characterization of the entire matrix of 24 connections is provided in the [supplemental information](#).

Inhibitory connectome of the claustrum: A disinhibitory toggle

To define local synaptic connectivity, voltage-clamp recordings were used to measure inhibitory postsynaptic currents (IPSCs) evoked by widefield photostimulation of presynaptic INs (Figures 1E–1G). We measured IPSCs, rather than IPSPs, to avoid the effects of nonlinear summation of postsynaptic potentials.²⁷ The median amplitude of IPSCs evoked by 1.2-ms light flashes (Figure 1H) ranged from 19.5 pA (VIP-to-IN) to 531 pA (PV-to-CC); 500-ms flashes evoked IPSCs that were longer-lasting, but similar in amplitude (Figure S2). IPSC latency was relatively similar across connections and ranged from 15.7 to 22.4 ms.

Photostimulation of PV-INs (Figure 1E) evoked IPSCs in nearly all claustral neurons (102/102 CC-PNs, 21/23 CS-PNs, and 26/33 INs). While the probability of receiving PV-IN input was high for all postsynaptic neuron types (Figure 1I), IPSCs in postsynaptic CC-PNs were significantly larger than those in CS-PNs or INs (Figures 1E–1H). Responses were not significantly different across subtypes of postsynaptic neurons within the CC-PN and IN categories, although responses in the PN2 subtype were larger than in INs (Figures S3A, S3D, and S3G).

Similarly, photostimulation of SST-INs almost always evoked IPSCs in postsynaptic neurons (73/74 CC-PNs, 11/11 CS-PNs, and 23/24 INs; Figure 1I). These IPSCs were comparable in time course to those evoked by photostimulation of PV-INs (Figure 1F) and were significantly larger in CC-PNs when compared to IPSCs measured in CS-PNs and PV-INs (Figure 1H). Responses were relatively consistent across subtypes of postsynaptic neurons within the CC-PN and IN categories (Figures S3B, S3E, and S3H).

IPSCs evoked by photostimulating VIP-INs (Figure 1G) were generally smaller than those resulting from photostimulation of PV-INs or SST-INs (Figures 1H, S2C, and S2D). This accounts for the more modest inhibition of postsynaptic AP firing produced by the activation of VIP-INs (Figure 1D2). VIP-INs preferentially inhibited other INs, rather than CC-PNs or CS-PNs (54/110 CC-PNs, 6/17 CS-PNs, and 31/44 INs). IPSCs evoked by brief photostimulation of VIP-INs were larger in postsynaptic CC-PNs than in INs (Figure 1G); responses to prolonged photostimuli (500 ms duration) were larger in INs (Figure S2), presumably due to differential effects of short-term synaptic plasticity at the two connections. For both short and long photostimuli, IPSCs were larger in INs than in CC-PNs. There were quantitative differences between some postsynaptic CC-PN and IN subtypes, indicating specialization in VIP-IN circuit computations (Figures S3C, S3F, and S3I).

These results indicate that claustral local inhibition is heterogeneous. The bias of each IN subtype toward its postsynaptic targets was calculated as the product of IPSC amplitude (Figure 1H) and response probability (Figure 1I), then normalized relative to the maximum for each IN subtype. This analysis revealed that PV-INs inhibit CC-PNs, SST-INs inhibit both PN types, and VIP-INs preferentially inhibit INs (Figure 1J).

(B–D) Inhibition of AP firing in postsynaptic neurons produced by photostimulation (1.2-ms duration, 4 flashes at blue bars) of (B1) PV-INs, (C1) SST-INs, or (D1) VIP-INs. Top traces show control responses to current pulses (bottom traces), while middle traces show inhibition of AP firing produced by IN photostimulation. (B2–D2) Relationship between stimulating current and AP frequency in the absence (black) and presence (red) of photostimulation of the INs indicated in (B1) to (D1). Postsynaptic neurons were PN2 (B2; $n = 9$), PN4 (C2; $n = 4$), and SST-IN (D2; $n = 11$), and AP frequency was measured between 250 and 500 ms after the start of depolarization. Points indicate mean values, and error bars are ± 1 SEM; smooth curves are fits of Boltzmann functions. 2-way repeated measure ANOVA indicated large effect sizes (η^2) for B2 and C2 and medium-large effect for D2; p values were 10^{-4} (B2), 0.02 (C2), and 0.048 (D2).

(E–G) IPSCs elicited by widefield photostimulation of (E) PV-INs, (F) SST-INs, or (G) VIP-INs, recorded in postsynaptic claustrum-cortical (CC) PNs, claustrum-subcortical (CS) PNs, and interneurons (INs). Dark traces indicate median values obtained from 3 to 24 experiments, shaded areas are \pm median absolute deviation; note different vertical scale for (G).

(H) Connection-specific amplitudes of light-evoked IPSCs. Points indicate IPSCs recorded in individual neurons, while bars indicate median values. Dunn's t test p values: * $p < 0.05$, ** $p < 0.01$, and *** $p < 0.001$.

(I) Connection probability, calculated from the ratio of number of neurons with light-evoked IPSCs/total number of tested neurons.

(J) Connection bias, calculated from the product of (H) and (I) and normalized to the largest value for each presynaptic IN type.

(K) Schematic of the inhibitory circuitry of the claustrum. Circles indicate INs, while triangles indicate PNs. Inhibitory connections are shown by red arrows, while disinhibitory VIP-PN connections are green. Arrow thickness indicates connection bias.

(L) Model simulation of IN effects on the activity of CC-PNs and CS-PNs. Bars and circuit diagrams at the top indicate activation of PNs (blue), PV/SST-to-PN connections (red), and disinhibitory VIP-to-PV/SST connections (green). CCs receive stronger inhibition but are also more disinhibited than CS neurons.

(M) Quantification of the predicted inhibition and disinhibition of CC-PNs and CS-PNs.

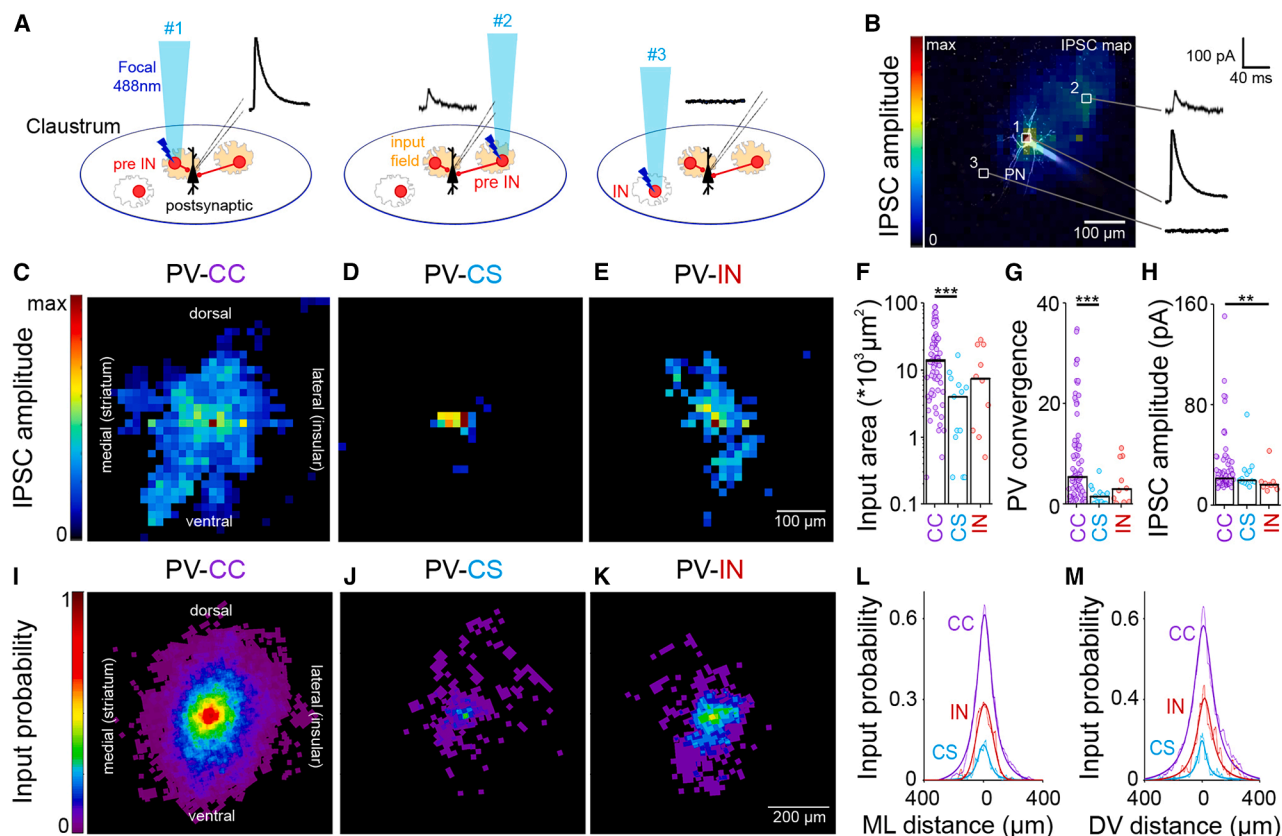


Figure 2. Spatial organization of claustral PV-IN connectome

(A) Schematic of the photostimulation procedure for inhibitory circuit mapping. A focal laser spot stimulated a presynaptic PV-IN (red) at a pixel location #1, while adjacent PV neurons were inactive. When the presynaptic IN fired an AP, an IPSC (black trace at top) was evoked in the postsynaptic PN and was registered to the location of the presynaptic IN. At location #2, a different presynaptic IN was stimulated, resulting in a smaller IPSC, while photostimulating the non-connected IN at location #3 did not generate an IPSC.

(B) Integrating responses across all photostimulation pixels generates a two-dimensional IPSC input map, reflecting the local inhibitory circuit. Hotter colors indicate larger IPSCs (calibration at left); representative IPSC traces at right. The structure of the dye-filled and patched PN is shown in white. Scale bar, 100 μm .

(C–E) Representative input maps for IPSCs evoked in CC-PNs (C), CS-PNs (D), and INs (E) in response to focal photostimulation of PV-INs. Scale bar, 100 μm . (F) Individual values (points) and medians (bars) of PV-IN input areas. Dunn's *t* test: ****p* = 0.001.

(G) Individual values (points) and medians (bars) for PV-IN convergence. Dunn's *t* test: ****p* = 0.001.

(H) Individual values (points) and medians (bars) of amplitudes of IPSCs evoked by focal photostimulation of PV-INs. Dunn's *t* test: ***p* = 0.003.

(I–K) Maps of PV-IN input probability for postsynaptic CC-PNs (I), CS-PNs (J), and INs (K). Hotter colors indicate higher connection probabilities (calibration at left). Scale bar, 200 μm .

(L) Spatial profile of PV inputs along the medio-lateral (ML) axis of indicated postsynaptic neuron types. (M) Spatial profile of PV inputs along the dorsoventral (DV) axis. Thin lines: raw data; thick lines: Gaussian fits. Sample sizes: PV-to-CC (75), PV-to-CS (13), and PV-to-IN (10).

These data establish the claustral inhibitory connectome (Figure 1K). To determine the function of these inhibitory circuits, a computational model based on the data in Figures 1 and S2 was used to simulate responses of PNs to excitatory input (Figure 1L). This input evoked an action potential in all claustral PNs and INs, while claustral output reflected the net activity of postsynaptic PNs following local circuit interactions. Selective PN activation yielded maximal activity (blue bar in Figure 1L), while additionally activating PV-IN/SST-IN strongly inhibited CC-PN and moderately inhibited CS-PNs (Figure 1L, red bar; Figure 1L, left). Concurrent activation of VIP-INs (Figure 1L, green bar) caused pronounced disinhibition of CC-PNs and smaller effects on CS-PNs (Figures 1L and 1M). Thus, the claus-

trum uses a familiar cortical VIP-IN motif^{28–30} for a novel function, namely to toggle output between its subcortical and cortical targets.

Structured PV-IN circuits spatially filter claustral communication

To map the spatial organization of claustrum inhibitory circuitry, we located presynaptic INs using a laser light spot that pseudorandomly photostimulated ChR2-expressing INs one pixel at a time (Figure 2A; see also Figures S4A and S4B and STAR Methods).²³ Because INs were larger than individual photostimulation pixels, multiple contiguous pixels could evoke action potentials in an IN (Figure S4B). The cumulative area of

photostimulation (optical footprint²³) was determined for each IN subtype from the pixels where the laser spot elicited APs (Figures S4B and S4C). Laser intensity was carefully adjusted for each subtype of ChR2-expressing presynaptic IN to ensure that action potentials were reliably generated when the laser light spot was positioned near their cell body (Figures S4B and S5A–S5C), while keeping laser power sufficiently low to avoid evoking action potentials when the light spot was positioned over their axons or distal dendrites (Figure S4B). Optical footprints were centered over IN cell bodies and ranged from 2,500 to 13,000 μm^2 (Figures S5D–S5F), corresponding to 1%–5% of the microscope field and a spatial resolution of approximately 40 μm for photostimulation.

Combining such focal photostimulation of ChR2-expressing presynaptic INs with patch clamp recordings of light-evoked IPSCs in postsynaptic neurons allowed mapping of local inhibitory circuits: pixels where light evoked an IPSC indicated the location of presynaptic INs (Figure 2A), so that maps correlating the amplitude of light-evoked IPSCs with pixel position revealed the spatial structure of presynaptic input onto individual postsynaptic neurons (Figures 2B and S4D–S4F). Such maps indicated that PV-IN inputs extended over hundreds of micrometers in each direction (Figures 2C–2E), meaning that presynaptic INs were both very close to and more distant from the cell bodies of their postsynaptic targets (at the center of each map). Input fields were elliptical—reflecting the dorso-ventrally elongated structure of the PV-IN-enriched claustral core³¹—and excluded the surrounding insular cortex. The maps of PV-to-CC circuits (Figures 2C and 2F) were significantly larger than those for PV-to-CS circuits (Figures 2D and 2F), while PV-to-IN maps were intermediate in area (Figures 2E and 2F).

Differences in input area largely reflect differences in the number of converging presynaptic neurons, allowing PV-IN convergence to be estimated by dividing the area of individual postsynaptic input fields (Figure 2F) by the presynaptic PV-IN optical footprint²³ (Figure S4C). Median PV-IN convergence ranged from 1.6 to 5.4, with significantly greater convergence of PV-INs onto CC-PNs than on CS-PNs (Figure 2G). Unitary IPSC amplitude was calculated from the mode of distributions of the amplitude of light-evoked IPSC and was similar for CC-PNs and CS-PNs (Figure 2H), but significantly smaller for INs. This emphasizes that CC-PNs, rather than CS-PNs or INs, are the primary target of PV-INs and reveals that the larger IPSCs of CC-PNs produced by widefield photostimulation of PV-INs (Figure 1H) arise from the convergence of more PV-INs onto CC-PNs.

To visualize the overall organization of PV-IN circuitry, we determined the probability of finding presynaptic PV-INs at a given position relative to their postsynaptic targets. This was done by aligning and averaging input maps from multiple experiments.²³ For all PV-IN circuits, input probabilities peaked near the postsynaptic neuron soma (center) and declined with distance (Figures 2I–2K). The dense probability map of CC-PNs (Figure 2I) indicates strong connectivity with both nearby and distant PV-INs and predominantly reflects PV-to-PN2 and PV-to-PN3 connections (Figures S6A–S6E). The small and weak probability map of CS-PNs (Figure 2J) indicates sparse inhibition by a few dispersed PV-INs. The probability map for PV-to-IN

circuits (Figure 2K) was like that of the PV-to-CC circuit (Figure 2I), but with an overall lower probability. PV-to-IN circuits mainly consisted of PV-INs innervating PV-INs and SST-INs (Figures S6F–S6H).

Input probability maps were quantified along the medio-lateral (Figure 2L) and dorsoventral axes (Figure 2M). PV-to-CS connections were the narrowest, while PV-to-CC and PV-to-IN connections spanned larger areas. All were more extensive in the dorsoventral axis, again mirroring the shape of the claustrum (Figure 2M). All claustral neurons received some PV-IN input within 100 μm of their cell bodies; this indicates short-range inhibition and, for the PV-to-IN circuit, local disinaptic disinhibition. At greater distances, CC-PNs were more likely than INs to receive PV-IN input, yielding net inhibition of these CC-PNs.

To discern the functional impact of circuit spatial organization, we developed a computational model that calculated the spatial range of synaptic interactions for each neuron along the width of the claustrum (see STAR Methods). This model predicted how PV-INs transform claustral responses to spatially structured excitatory input. We first considered spatially uniform input (Figure 3A). PN responses were simulated both in the absence (black in Figure 3A1) and presence (purple/cyan in Figure 3A1) of PV-IN connections. As in the non-spatial model above (Figure 1L), claustrum output was calculated as PN activity in the presence of PV-IN inhibition, while inhibition (red in Figure 3A1) was the difference between PN responses with/without PV-IN inhibition. The stronger inhibition of CC-PNs by PV-INs (Figures 1 and 2) reduced the CC-PN output more than the CS-PN output (Figure 3A1) and yielded a lower output/input ratio for CC-PNs than for CS-PNs (Figure 3A2). Varying the amount of excitatory input caused proportional changes in both PN and IN activity (Figures S6K and S6L). Because both PN activation and PV-IN-mediated inhibition scaled with input strength, the output/input ratio, representing neuronal gain,^{32,33} remained constant across different input levels (Figure S6M) and was lower for CC-PNs than for CS-PNs (Figure 3A3).

Because responses of claustrum neurons to excitatory input are highly non-uniform,^{4,34} we next modeled the effects of intermingling strong and weak input (Figure 3B, black) that, on average, was comparable in strength to that in Figure 3A. The preferential connectivity of PV-INs to CC-PNs (Figures 1 and 2) caused CC-PN output to decrease by 27.6%, while CS-PN output decreased by only 6.9% (Figure 3B2). Notably, despite considerable spatial variability in presynaptic IN activity (SD = 2.24–2.37), postsynaptic inhibition across PNs was more spatially uniform (SD = 0.02–0.06; Figure 3B1, red). This uniformity of inhibition indicates that differences in individual PV-IN activity are spatially filtered across the claustrum. Because neighboring PNs receive similar inhibitory input, PNs receiving weak excitatory input are silenced (output/input = 0 in Figure 3B2). Such *spatial filtering* effects arise from the broad (hundreds of μm) connectivity observed between PV-INs and PNs (Figures 2 and S6N). Moreover, spatial filtering yields nonlinear effects on network gain, generating a high-pass amplitude filter that selectively suppresses weakly activated neurons (Figure 3B3). Such *amplitude filtering* also selectively reduced the variability of CC-PN output, with the SD of CC-PN output lower (1.11) than that of CC input (1.16). This effect was absent

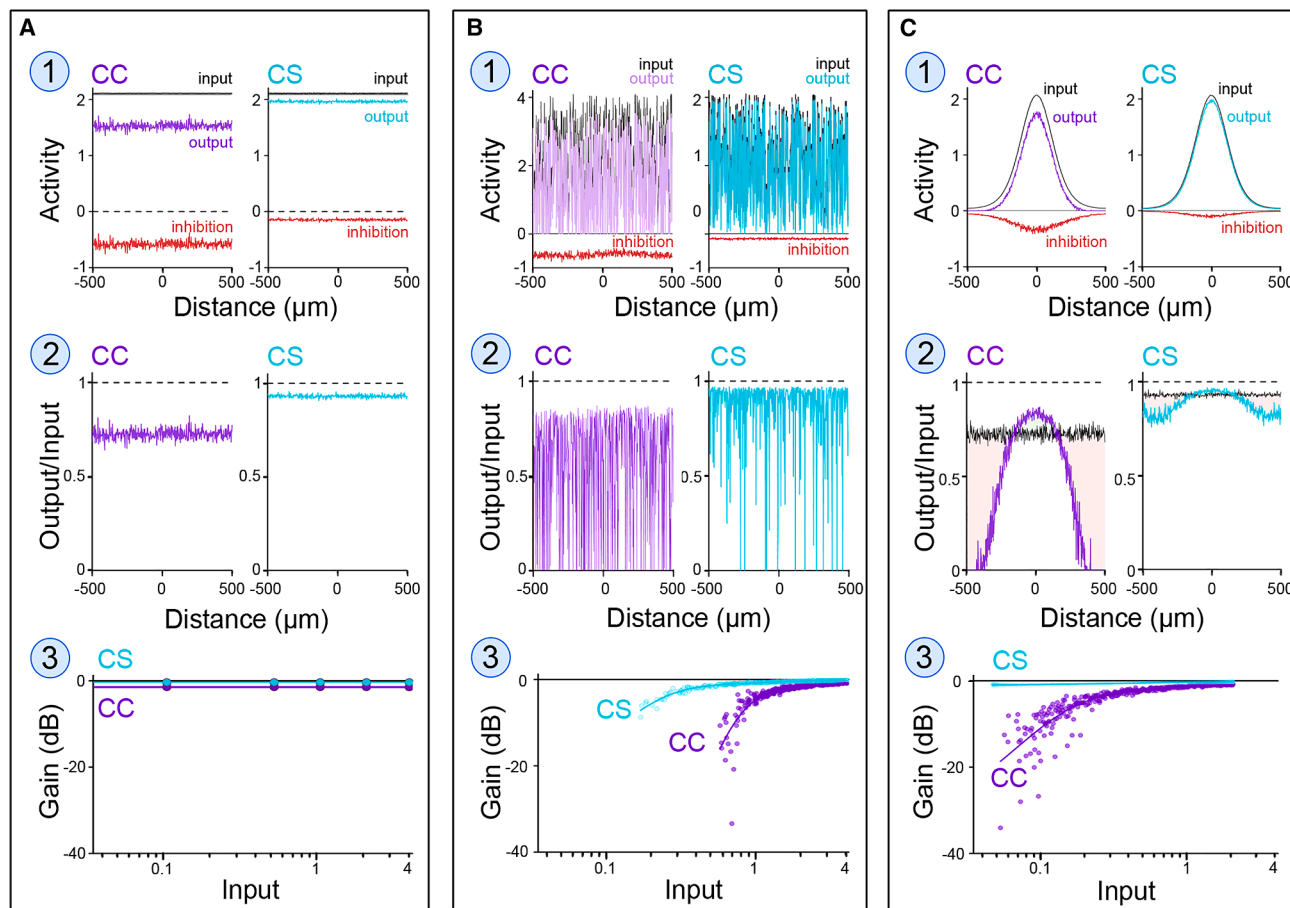


Figure 3. Modeling the effects of PV-IN circuits on claustral output

Network simulations probed the effects of inhibition mediated by PV-INs on claustral response to excitatory inputs that were spatially homogenous (A), spatially heterogeneous (B), or spatially tuned (C). (A1) Identical, uniform inputs (black) result in spatially uniform inhibition that was larger for CC-PNs (red), yielding smaller output for CC-PNs (violet) compared to CS-PNs (teal). (A2) Ratio of output/input for both PNs. (A3) Network gain (output/input ratio) was uniform, regardless of input strength, but smaller for CC-PNs than for CS-PNs. (B1) Spatially heterogeneous inputs (black) were filtered by PV-INs to yield relatively constant levels of postsynaptic inhibition (red). Inhibition was larger for CC-PNs than for CS-PNs, and output was lower for CC-PNs (violet) than for CS-PNs (teal). (B2) Constant inhibition and highly variable input resulted in output/input ratios that vary widely, with some inputs entirely blocked (zero values). (B3) Spatial filtering of heterogeneous inputs by PV-INs yielded nonlinear reductions in claustral output that efficiently blocked weak inputs. Such high-pass filtering was greater for CC-PNs. (C1) Spatially tuned input (black) resulted in maximum inhibition (red) and output (violet/teal) at the center and is reduced at the input periphery. (C2) At the input center, spatially tuned input reduced the output/input ratio less than a uniform input (black, from panel A2), while the peripheral output/input ratio was smaller than for uniform input. These peripheral effects were sufficient to eliminate CC-PN output, but not CS-PN output. (C3) Spatially tuned input resulted in nonlinear gain that was lower for weak inputs and higher for large inputs.

in CS-PNs (input and output SD both 1.19), due to weaker PV-IN inhibition. In summary, the combination of non-uniform excitation and broad PV-IN inhibition causes the claustrum to nonlinearly filter its output to cortical targets.

To evaluate the spatial filtering properties of claustral PV-IN circuits, excitatory inputs were next spatially tuned across the claustrum (Figure 3C1, black) to simulate the distribution of cortical input across different parts of the claustrum.¹⁷ Inhibition mirrored the spatial input profile, peaking at the center and declining toward the periphery (Figure 3C1, red). Network output (Figure 3C1, violet/teal) similarly tracked input (Figure 3C2). However, two notable features emerged. First, the output at the center (Figure 3C2, violet) exceeded that produced by uniform excitatory input (Figure 3C2, black)

despite equivalent central input in both cases. This paradoxical increase in central output was a consequence of central PNs receiving less inhibition from less-active peripheral PNs (Figure S6O). Second, peripheral CC-PNs were largely inactive (Figure 3C2) because their lower excitatory drive was further reduced by inhibition from central INs (Figure S6O). Thus, the PV-IN network acts as an *active* spatial filter, relatively boosting CC-PN output in the center while suppressing it in surrounding regions. These effects increased as excitatory inputs were more spatially restricted (Figures S6P and S6Q) and again were less pronounced in CS-PNs (Figure 3C2, right). Similar effects were observed in response to input that was spatially tuned, but noisy (Figures S6R–S6T). Thus, active spatial filtering by PV-INs boosts relative claustral

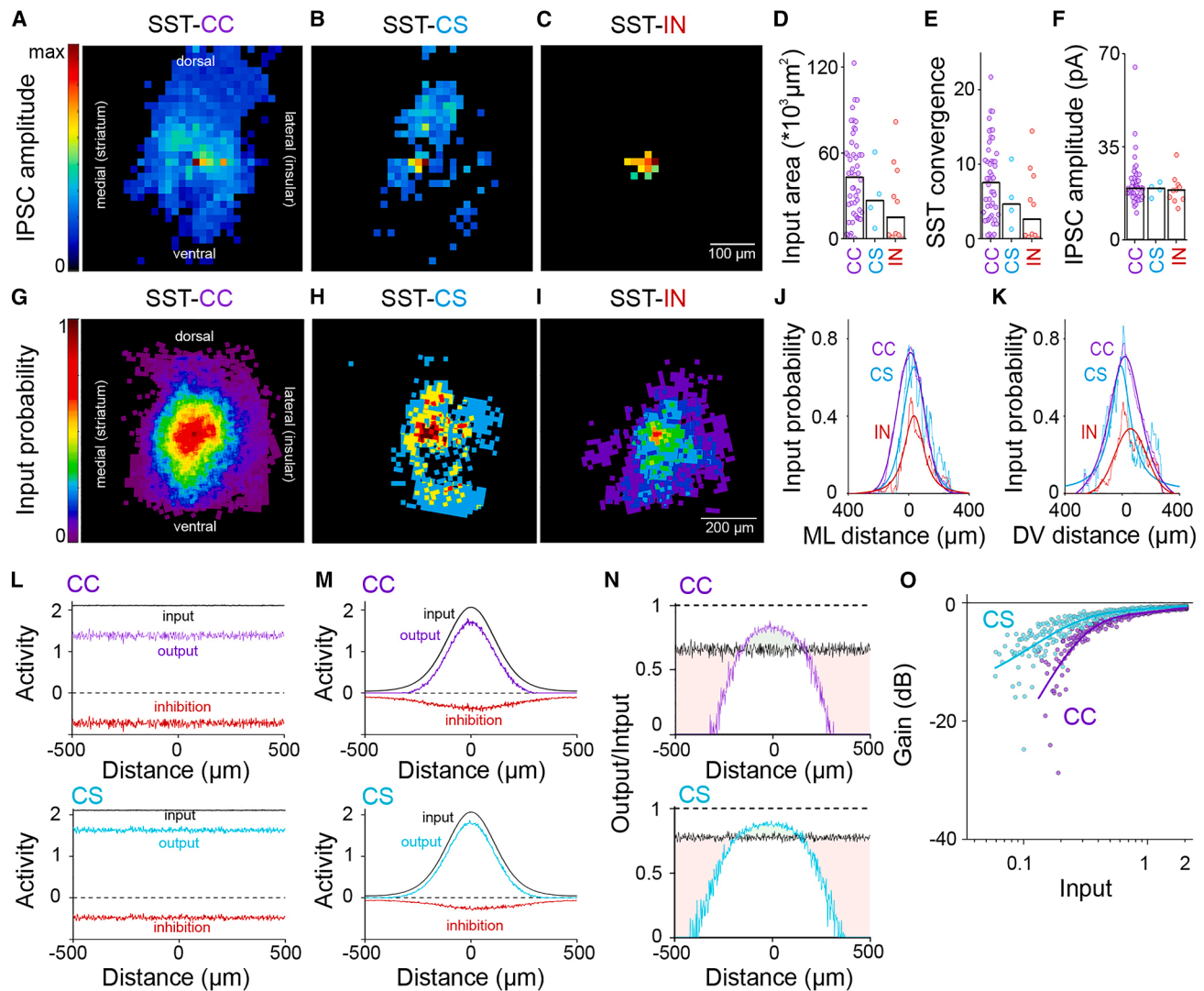


Figure 4. Spatial organization of SST-IN functional connectome

(A–C) Representative maps of IPSCs evoked in postsynaptic CC-PNs (A), CS-PNs (B), and INs (C) in response to focal photostimulation of presynaptic SST-INs. Hotter colors indicate larger IPSCs (calibration at left). Scale bar, 100 μm .

(D) Individual values (points) and medians (bars) of the area of SST-IN input fields. Dunn's *t* test indicated no significant differences between groups.

(E) Individual values (points) and medians (bars) of SST-IN convergence. Dunn's *t* test indicated no significant differences between groups.

(F) Individual values (points) and median values of IPSC amplitudes evoked by focal photostimulation of SST-INs. Dunn's *t* test indicated no significant differences between groups.

(G–I) Maps of SST-IN input probability for CC-PNs (G), CS-PNs (H), and INs (I). Hotter colors indicate higher connection probabilities (calibration at left). Scale bar, 200 μm .

(J) Spatial profile of SST-IN input to postsynaptic neurons along the medio-lateral (ML) axis.

(K) Spatial profile of SST-IN input along the dorsoventral (DV) axis. Thin lines: raw data; thick lines: Gaussian fits.

(L and M) Simulated effects of spatially uniform (L) and spatially tuned (M) excitatory inputs.

(N) Predicted output/input ratio for SST-IN circuits of CC-PNs and CS-PNs. When compared to a uniform input (black line, from L), spatially tuned inputs yielded a strong reduction in peripheral output from both CC-PNs and CS-PNs, while central outputs were increased.

(O) Gain of CC-PN and CS-PN circuits are both nonlinear, with strong attenuation of weak inputs. Sample sizes: SST-to-CC (50), SST-to-CS (4), and SST-to-IN (10).

output in regions of strong excitatory input, while amplifying inhibition and reducing output for areas receiving weak input (Figure S6O). This imparts nonlinear gain onto PV-IN circuits with CC-PNs (Figure 3C3).

Spatial filtering by SST-IN inhibitory circuits

The same approach enabled analysis of claustral SST-IN circuitry. SST-IN input fields were elliptical and widest along the dorsoventral axis (Figures 4A–4C), like PV-IN circuits (Figure 2). However,

both CC-PNs and CS-PNs exhibited substantially larger SST-IN input fields than those of PV-IN inputs (compare Figures 4A–4D to Figures 2C–2F). This difference arose from at least three causes: (1) while PV-INs are mostly in the claustrum core, SST-INs are present in both core and shell^{26,35}; (2) SST-INs converged on their targets more than PV-INs did: SST-IN convergence ranged from 2.7 to 7.6 (Figure 4E); and (3) unlike PV-INs (Figure 1G), SST-INs robustly inhibited CS-PNs. SST-to-IN circuits exhibited smaller input fields and less convergence than SST-to-PN circuits, although these differences were not statistically significant (Figures 4C–4E). No differences in unitary IPSC amplitudes were observed between SST-IN targets (Figure 4F).

While the probability of presynaptic SST-IN input was highest near the somata of all three postsynaptic neuron types, differences in circuit spatial organization were observed (Figures 4G–4I). SST-to-CC connections were more widespread than those of SST-to-CS or SST-to-IN (Figures 4J and 4K), largely due to strong input onto PN2, PN4, and PN5 subtypes (Figures S7A–S7J). The maximum connection probability for CC-PNs and CS-PNs was approximately twice that of INs (Figures 4J and 4K).

Computational modeling revealed the functional consequences of these SST-IN circuits. With spatially uniform excitatory input (Figure 4L, black), both CC-PNs and CS-PNs were strongly inhibited (Figure 4L, red), unlike PV-INs (Figure 3A). Spatially tuned input caused SST-INs to produce location-specific inhibition of both PN types (Figure 4M), with inhibition relatively small at the input center and greater at the periphery (Figure 4N). This active spatial filtering produced nonlinear gain changes that preferentially attenuated weak inputs (Figures 4N and 4O). Thus, SST-INs also function as high-pass amplitude filters that sharpen spatial boundaries. One unique feature of local SST-IN circuits was that inhibition of CS-PNs was disproportionately lateral (Figure 4J) and yielded asymmetrical inhibition of these PNs (Figures S7K–S7P).

Spatial organization of VIP-IN disinhibitory circuits

We also determined the spatial organization of claustral VIP-IN circuits. A relatively sparse connectivity between VIP-INs and their postsynaptic targets was apparent in noisy input maps (Figures 5A–5C). These maps were also smaller in area (Figure 5D) than those associated with PV-IN and SST-IN circuits. VIP-IN convergence (Figure 5E) was similar amongst the three postsynaptic targets; convergence values of ~ 1 indicated roughly 1-to-1 connections between VIP-INs and their targets. Because unitary IPSC amplitudes were also similar for the three postsynaptic targets (Figure 5F) and nearly comparable to those produced by PV-INs and SST-INs, the relatively small IPSCs observed during widefield photostimulation of VIP-INs (Figure 1G) are a consequence of very low convergence of VIP-INs onto their targets.

Input probability maps revealed that presynaptic VIP-INs were widely scattered, with distributions that varied according to postsynaptic target type (Figures 5G–5I). For PNs, input probability was low (Figures 5G, 5H, 5J, and 5K); the VIP-to-IN circuit was similar in shape but with higher peak probability (Figures 5I–5K). VIP-IN input to PN2 was comparable to that received by INs, suggesting PN subtype-specific VIP-IN functions (Figures S8A–S8J).

VIP-IN preferential inhibition of other INs was reflected in wider connectivity to INs than to PNs (Figures 5J and 5K), without clear IN subtype preferences (Figures S8A–S8J).

Simulations revealed that the physiological actions of VIP-INs depend upon postsynaptic PN type. For CC-PNs, direct VIP-IN inhibition was outweighed by disynaptic disinhibition, resulting in a small net disinhibition (green in Figure 5L, top). In contrast, CS-PNs received greater direct inhibition from VIP-INs, causing a mild net inhibition (red in Figure 5L, bottom). Spatially biased excitatory input (Figure 5M) was minimally affected in its center, while more prominent effects occurred in peripheral PNs: CC-PNs increased their output, while CS-PN output decreased (Figure 5N). Thus, VIP-INs are active filters that selectively control weaker signals: they are low-pass amplifiers for CC-PNs and high-pass filters for CS-PNs (Figure 5O). These differential actions of VIP-INs should bias claustral output toward cortical, rather than subcortical, targets.

Different contributions of INs to claustral input processing

We next compared the predicted ability of circuits formed by different presynaptic INs to influence claustral output. For uniform excitatory input (Figure 6A1), IN inhibition of CC-PNs was greater for SST-IN circuits than for PV-IN circuits (Figure 6A2). Although the unitary IPSCs elicited in CC-PNs by focal photostimulation of SST-INs and PV-INs were similar in amplitude (Table S1), the larger inhibition produced by SST-INs arose from their broader spatial connectivity and higher convergence onto CC-PNs (Figures S9A and S9D). Despite the robust inhibition of CC-PNs by SST-INs and PV-INs (Figure 1H) and preferential inhibition of these INs by VIP-INs (Figures 5I–5K), VIP-INs minimally disinhibited the CC-PN output (0.57% increase; Figure 6A2). This presumably reflects the omission of spatial filtering effects. In contrast, CS-PNs were primarily inhibited by SST-INs, with only weak inhibition from PV-INs and VIP-INs (Figure 6A3).

To compare active spatial filtering by claustral INs, we examined their effects on responses to spatially tuned input (Figure 6B1). Central inhibition was mild and comparable for SST-INs and PV-INs (Figure 6B2), despite the larger inhibitory effects of SST-INs on CC-PNs (Figure 6A2). However, SST-INs narrowed CC-PN output more (Figure 6B2), due to stronger inhibition by peripheral SST-INs. In CS-PNs, sparse connectivity from PV-INs and VIP-INs resulted in minimal inhibition, with only SST-INs efficiently suppressing CS-PN output (Figure 6B3).

In summary, PV-INs act as active spatial filters that selectively promote transmission of strong excitatory signals to cortical targets via CC-PNs while minimally affecting subcortical outputs via CS-PNs (Figure S10A). Though SST-INs exhibit filtering properties similar to those of PV-INs, SST-INs enable selective transmission of strong excitatory input to both cortical and subcortical targets (Figure S10B). VIP-INs modulate weak input in a PN-specific manner, enhancing CC-PN output while reducing CS-PN output, thereby toggling between these pathways (Figure S10C). Thus, each IN subtype exerts unique effects upon information flow from the claustrum to its cortical and subcortical targets.

We also incorporated the combined actions of all 3 types of INs into our spatial model to simulate normal physiological

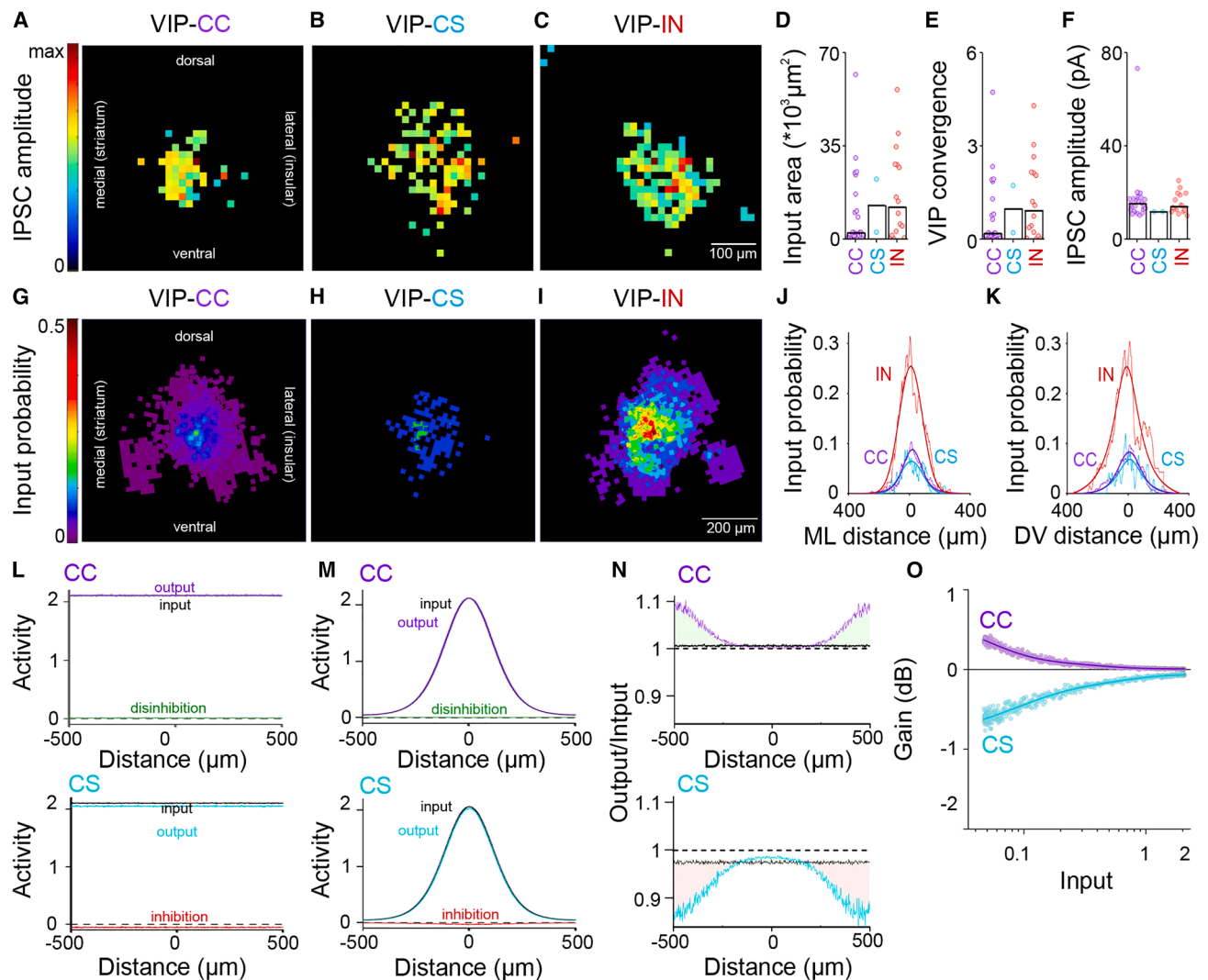


Figure 5. Spatial organization of claustral VIP-IN connectome

(A–C) Representative maps of IPSCs evoked in postsynaptic CC-PNs (A), CS-PNs (B), and INs (C) in response to focal photostimulation of presynaptic VIP-INs. Hotter colors indicate larger IPSCs (calibration at left). Scale bar, 100 μm .

(D) Individual values (points) and medians (bars) of areas of VIP-IN inputs onto the indicated postsynaptic targets. Dunn's *t* test indicated no significant differences between groups.

(E) Individual values (points) and medians (bars) of VIP-IN convergence. Dunn's *t* test indicated no significant differences between groups.

(F) Individual values (points) and medians (bars) of IPSC amplitudes evoked by focal photostimulation of VIP-INs. Dunn's *t* test indicated no significant differences between groups.

(G–I) Maps of VIP-IN input probability for CC-PNs (G), CS-PNs (H), and INs (I). Hotter colors indicate higher connection probabilities (calibration at left). Scale bar, 200 μm .

(J) Spatial profile of VIP-IN input along the medio-lateral (ML) axis.

(K) Spatial profile of VIP-IN input along the dorsoventral (DV) axis. Thin lines: raw data; thick lines: Gaussian fits. Sample sizes (number of neurons with IPSCs/number of tested neurons: VIP-to-CC [26/82], VIP-to-CS [2/12], VIP-to-IN [16/23]).

(L–O) Simulated effects of spatially uniform (L) and spatially tuned (M) excitatory inputs. CC-PNs are disinhibited (green), while CS-PNs are inhibited (red).

(N) Output/input ratio for VIP-IN circuits of CC-PNs and CS-PNs. When compared to uniform input (black line, from L), spatially tuned inputs led to disinhibition and larger outputs for CC-PNs, but the reverse for CS-PNs. Effects were the largest for weak inputs.

(O) Network gain was positive for CC-PNs and negative for CS-PNs, with larger effects for smaller inputs in both cases. VIP-INs act as mild low-pass amplifiers for CC-PNs and high-pass filters for CS-PNs.

conditions. Quantitatively, claustrum cortical output was reduced by approximately 40% (Figure 6C1, violet), yielding a ratio of output/input that was lower than that produced by any in-

dividual IN type (compare Figures 6C2 to 6B2). In contrast, peak inhibition of CS-PNs by all INs was approximately 20% (Figure 6C1, cyan) and nearly identical to that produced by

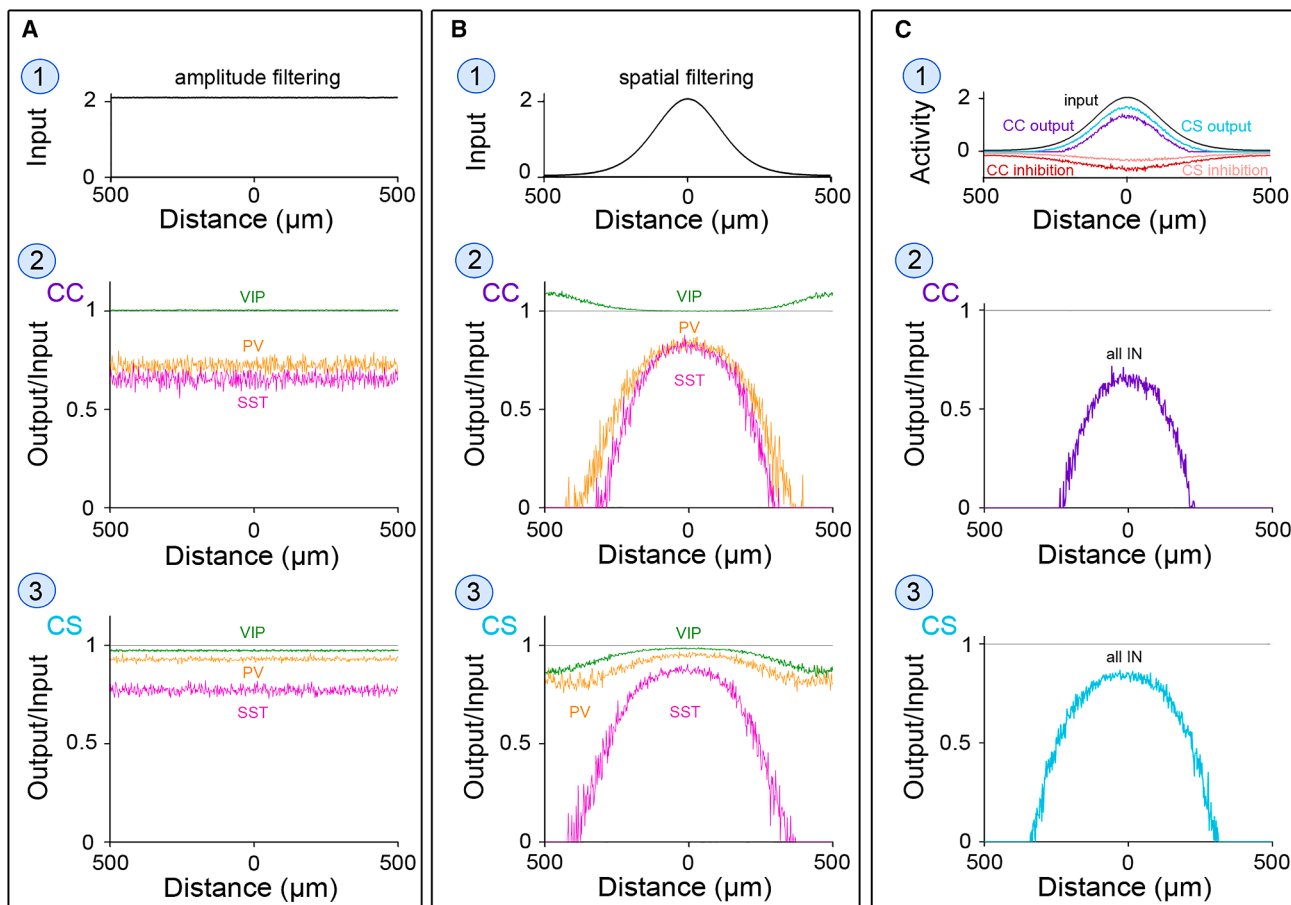


Figure 6. Comparison of filtering properties of claustral IN circuits

(A) Simulated effects of INs on output/input ratios for responses to spatially uniform excitatory input (A1) of CC-PNs (A2) and (A3) CS-PNs. Output/input ratio depended on the presynaptic IN type and differed between PV-INs (orange), SST-INs (magenta), and VIP-INs (green).

(B) Output/input ratios for responses to spatially tuned inputs (B1) in CC-PNs (B2) and (B3) CS-PNs. VIP-INs are disinhibitory for CC-PNs, with the largest effects in the periphery, while inhibitory for CS-PNs.

(C) Simulated modulation of PN outputs by the combined activity of all three IN types. (C1) Spatially tuned input yields larger output for CS-PNs than for CC-PNs. (C2) Combined IN activity yielded less output for CC-PNs than when only single IN types were active and a more sharply tuned output/input curve. (C3) Inhibition of CS-PNs by the combined actions of all INs was relatively mild, particularly at the center of the output/input curve, but with sharper spatial tuning than when single IN types were active.

SST-INs alone. Inhibition was greater at the periphery, due to the additional inhibitory effects of PV-INs and VIP-INs (Figures 6B3 and 6C3).

Experimental tests of spatial filtering model

To validate our computational model, we tested its predictions with experiments that examined claustral responses to excitatory input. Specifically, we tested the model version that included contributions from all three IN subtypes and focused on CC-PNs, the most abundant PN class whose output is predicted in Figure 6C2.

To test model predictions, ChR2 was expressed in the anterior cingulate cortex (ACC), one of the key cortical inputs to the claustrum.^{17,20,36} An AAV that expresses ChR2-eYFP under the control of the PN-specific Camk2 promoter was injected into the ACC (Figure 7A) and ChR2 was anterogradely expressed

in claustral ACC inputs, as visualized by the eYFP tag on the ChR2 (Figure 7B). These inputs were densest in the center of the claustrum (Figure 7C), reflecting preferential ACC innervation of the claustrum core relative to the claustrum shell.^{17,20,36,37}

Consistent with both previous experiments^{20,36,38} and our model, photostimulating ACC inputs (1.2 ms duration) evoked action potentials in both postsynaptic PNs and INs (Figure 7D). Voltage-clamp recordings indicated that ACC input excited PNs and INs by producing excitatory postsynaptic currents (EPSCs; Figure 7E). Like the distribution of ChR2-YFP (Figure 7C), these EPSCs were largest at the input center and declined with distance (Figure 7F). Because ACC input excited both PNs and INs (Figure 7G, left), these inputs also evoked synaptic inhibition in PNs: blocking IN-mediated inhibition with the GABA_A receptor antagonist gabazine (Gbz, 10 μM) increased EPSC amplitude (Figure 7G, top). Subtracting EPSCs recorded

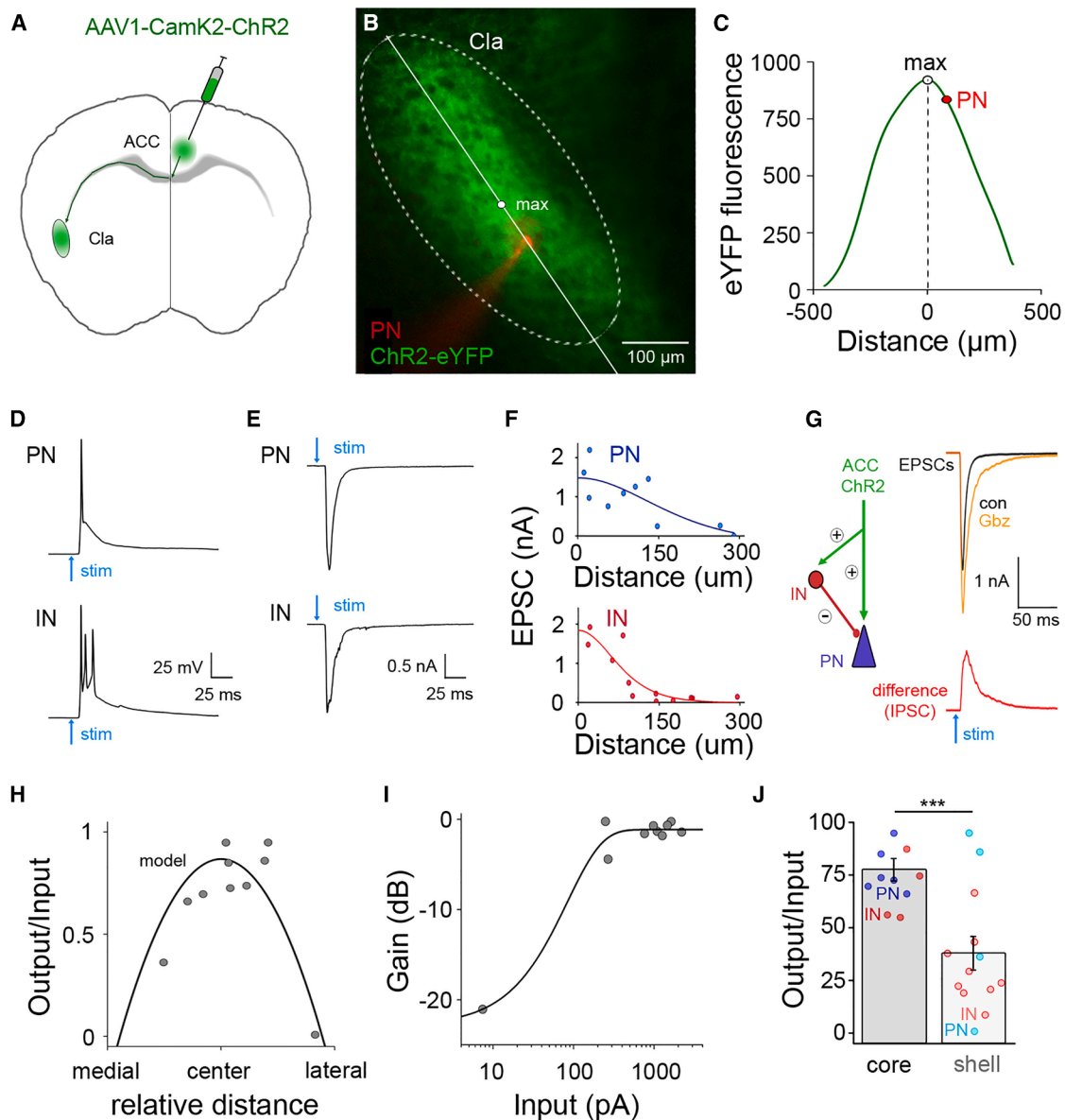


Figure 7. Local INs spatially filter excitatory ACC input to the claustrum

(A) Injecting AAV1-CamKII-ChR2-YFP virus into the ACC expressed YFP-tagged ChR2 in excitatory axons innervating the claustrum.
 (B) Fluorescence image of ChR2-eYFP (green) in axonal projections from the ACC within the claustrum, along with a patched CC-PN (red). White line indicates the location of the eYFP intensity line plot in (C); it intersects both the input maximum (max; white point) and the patched CC-PN. The dashed line indicates the approximate boundary of the claustrum core. Scale bar, 100 μ m.
 (C) Spatial profile of eYFP fluorescence for the experiment shown in (B). Location of the patched neuron, relative to the input peak (max), is indicated by the red point (PN).
 (D) AP firing in a CC-PN (top) and an IN (bottom) after widefield photostimulation (1.2 ms duration, at arrows) of ChR2-expressing ACC axons.
 (E) EPSCs recorded from a CC-PN (top) and an IN (bottom) in response to photostimulation of ACC axons at the time indicated by arrows.
 (F) Relationship between EPSC amplitude and distance from input maximum for CC-PNs (top) and INs (bottom).
 (G) Quantification of local inhibition and output/input ratios. Left: ACC axons activate CC-PNs (PN) and INs, which in turn inhibit CC-PNs. Right: after blocking local inhibition with Gabazine (Gbz, yellow), EPSCs increased (top) and the difference between these two traces revealed the waveform of photostimulation-evoked IPSCs (bottom, red). The ratio of EPSC amplitudes measured in the presence and absence of Gbz defined the output/input ratio.
 (H) Output/input ratio for 10 claustral CC-PNs. This ratio was largest at the center of ACC input and smallest in the periphery (points) and aligned well with model predictions (smooth curve).
 (I) Gain of CC-PNs was higher for large EPSCs and lower for small EPSCs, demonstrating the predicted high-pass amplitude filtering properties of the claustrum.
 (J) Output/Input ratio for core and shell regions.

(legend continued on next page)

in the absence and presence of Gbz treatment revealed the disynaptic IPSC produced in PNs by INs (Figure 7G, bottom).

We tested our model by comparing the output/input ratio of PNs at different locations across the claustrum. This ratio was determined via EPSC amplitudes, with input defined as the amplitude of EPSCs measured in the presence of Gbz and EPSCs measured without Gbz treatment reflecting IN-modulated output (Figure 7G). To account for mouse-to-mouse variations in the distribution of ChR2-expressing ACC input, ChR2-YFP fluorescence was measured in each experiment, and the position of patched CC-PNs was referenced to the location where ChR2-YFP was maximal (Figure 7C). The distribution of ChR2-YFP was also used to define the spatial distribution of ACC input in our computational model.

We found a good correspondence between model predictions and claustral responses to ACC input. First, measurements from 10 CC-PNs exhibited the predicted bell-shaped relationship between claustrum output/input (points in Figure 7H). Thus, local inhibition had the smallest effect on ACC input that already was the strongest, as predicted. Second, the amount of attenuation of excitatory input by the claustrum (points in Figure 7H) quantitatively aligned with model predictions (curve in Figure 7H). Further, claustrum gain also depended on input strength, as predicted by the model (Figure 7I). The correspondence between model predictions and these experimental measurements validated the model.

To relate our findings to claustrum anatomy,^{17,20,36,37} we compared the output of the claustrum core and shell by using ACC axons to define the claustrum core (YFP fluorescence > 50% maximum) and shell (YFP < 50% maximum). While core neurons received greater excitatory input than shell cells, the relative amount of inhibition—determined by the degree of enhancement produced by Gbz—appeared larger in the shell (Figure S11). This caused the output/input function of the shell to be significantly lower than that of the core (Figure 7J), just as predicted by the model. We expect this to be reversed for input from the auditory cortex and orbitofrontal cortex, which preferentially innervate the shell.¹⁷

In summary, both our model predictions and experimental results demonstrated that the local inhibitory connectome of the claustrum implements input-dependent spatial filtering and selectively prevents transmission of weak input out of the claustrum.

DISCUSSION

An increasing number of behavioral studies have implicated the claustrum in a wide variety of cognitive processes. However, until now, there has been minimal information about how local computations within the highly interconnected claustrum transform the multitude of inputs that it receives. We have addressed this knowledge gap by employing a “bottom-up” approach to investigate the structure and function of claustral local circuitry. We comprehensively quantified inhibitory and disinhibitory circuit motifs, which then powered a computational model that defined

the roles of IN subtypes in local information processing. Comparison of model predictions with experimental observations confirmed the hypothesized network computations and revealed that the claustrum serves as a filter that precisely converts excitatory input targets into output to cortical and subcortical targets. Such filtering capabilities could explain how the claustrum is able to contribute to diverse cognitive processes.

Mapping and modeling claustral IN circuits

By selectively photostimulating each major IN subtype while recording from identified postsynaptic cell types,²⁶ an established optogenetic circuit-mapping technology^{23–25} allowed us to resolve claustral inhibitory circuits at near cell-pair resolution. This method is optimal for mapping inhibitory networks because of the minimal risk of polysynaptic activation. Our functional connectomics approach characterized 24 interneuronal circuits, thereby substantially extending previous studies limited to PV-to-CC synapses^{20,39} and providing an unprecedented view of claustrum IN circuitry.

To interpret our high-content data, we developed a comprehensive computational model of claustrum circuit function.⁴⁰ This model allowed us to measure and analyze inhibitory effects and disinhibitory effects (which are notoriously difficult to measure) as well as to define the individual functions of each IN subtype. These simulations also predicted how excitatory input affects claustral output; subsequent experimental measurements of responses of claustrum PNs to excitatory ACC input validated model predictions. Our analysis of the main connectivity motifs of the claustrum—with PV-INs and SST-INs primarily targeting PNs and VIP-INs preferentially innervating other INs, as well as broad convergence of these INs on the postsynaptic targets—illuminates how local connectivity can shape signal processing and input-output transformations. Because these inhibitory motifs are conserved throughout the brain,⁴¹ the relatively simple organization of the claustrum makes it a very suitable place to analyze the general functions of such network computations.

Claustrum as a filter

Our analysis revealed the emergent filtering properties of claustral inhibitory circuits. Remarkably, such nonlinear filtering only affects claustrum gain for spatially non-uniform input (compare Figures 3A3 and 3C3) and arises from convergence of dispersed INs onto PNs. This confers both amplitude and spatial filtering properties to the claustrum.

Amplitude filtering

Heterogeneous excitatory input intermixes active and inactive neurons, so that IN convergence yields nonlinear amplitude filtering: PNs receiving strong excitation are favored, while those with weak input are effectively suppressed (Figures 3B3 and S6N). Such filtering was anticipated by *in vivo* observations that the activity of individual claustral neurons can be either increased or decreased by incoming input.^{4,34} Given that claustral activity is upregulated prior to cognitive tasks,^{3,4,34} stronger inputs likely carry task-relevant information, whereas weaker

(J) Comparison of output/input ratio for neurons in the core or shell of the claustrum. While input EPSCs were smaller in shell CC-PNs (blue) and INs (red), the degree of local inhibition that these cells received was greater, yielding a significantly lower output/input ratio in the shell. Points indicate individual values, bars show means, error bars indicate \pm SEM, and *** indicates a significant difference between the core and shell ($p = 0.001$, Dunn's t test).

signals may represent less relevant “noise.” Thus, by suppressing weak inputs and preserving strong inputs, claustrum filtering can differentiate relevant signals from noise.

Spatial filtering

PN integration of inhibition from multiple presynaptic INs also yields nonlinear spatial filtering. Such effects relatively increase output from regions with strong excitatory input, while regions with weak input are suppressed. These filtering effects arise from the actions of both nearby and distant INs to PNs receiving weak excitatory input (Figure S6O), generating center-surround inhibition that enhances the relative output of highly activated claustral PNs and improves signal-to-noise ratio. Because claustral inputs are topographically arranged with gradual transitions between zones,^{17,36} this arrangement could sharpen functional boundaries and optimize input-specific signal processing.

In summary, claustral INs act as high-pass filters that efficiently suppress transmission of weak input signals while only mildly affecting the output of PNs that receive strong input. The exception is VIP-to-CC connections, which disinhibit and thereby mildly increase CC-PN activity.

Potential implications of claustrum filtering

Although we have considered claustrum circuits at the cellular level, our conclusion that the claustrum serves as an active filter is likely to have significant implications for the higher-order functioning of the claustrum. Specifically, because the claustrum is reciprocally connected to most cortical areas, a noise filtering cortico-claustral loop will increase task-relevant information while removing weaker noise signals. This hypothesis is supported by evidence that disrupting claustrum activity leads to cortical ensembles with a larger fraction of weakly activated neurons,⁴² as expected for impaired filtering. As a noise filter, the behavioral contributions of the claustrum should be most apparent under noisy conditions. Consistent with this prediction, claustral disruption minimally affects well-trained or innate behaviors but impairs performance in tasks with distractors.² In naive mice, task-specific neural ensembles are not yet established, and claustral activity increases during early learning,⁷ a critical time for cue-behavior associations. At this stage, noise filtering could enhance learning by distinguishing relevant from irrelevant cues. Indeed, early-stage claustral perturbations selectively disrupt behavior and delay learning, while perturbations at later stages have little effect.⁷ Moreover, findings that the claustrum encodes premotor information related to an impending task⁴ suggest that by filtering weak inputs and providing targeted feedback, the claustrum minimizes interference from non-task-related signals and reduces impulsivity.

In summary, results ranging from synaptic to behavioral support the concept that the claustrum optimizes cognitive function by serving as a filter to preferentially transmit strong, task-relevant signals. Such a mechanism could account for the otherwise puzzling roles of the claustrum in very diverse behavioral functions, such as associative learning,^{6,7} attentional allocation and impulsivity,^{1–3,5} and behavioral choice optimization.^{4,42}

Limitations of the study

While our experimental measurements in brain slices provide a detailed picture of the properties of claustrum inhibitory circuits,

future work will be needed to establish the spatial organization and detailed functional attributes of local excitatory circuits.³⁸ Likewise, additional *in vivo* work will be needed to test whether the claustrum can toggle its output between cortical and subcortical areas, as our model predicts, and whether the proposed filtering role of the claustrum is relevant for the numerous behavioral roles attributed to the claustrum. Finally, while our computational model of claustrum circuitry is the most advanced to date, future iterations could be improved by including the intrinsic electrical properties of individual neuron subtypes into the model to fine-tune response characteristics of specific cell types.

RESOURCE AVAILABILITY

Lead contact

Further information and requests for materials and data should be directed to and will be fulfilled by the lead contact, George J. Augustine (george_augustine@tli.org.sg).

Materials availability

This study did not generate any new materials.

Data and code availability

- All animal data reported in this paper will be made available upon request by the lead contact.
- All original code generated in the analysis of this study is available online at https://figshare.com/articles/software/Claustrum_Codes/30435856 and at <https://doi.org/10.6084/m9.figshare.30435856.v1>
- Any additional information required to reanalyze the data reported in this paper is available from the lead contact upon request.

ACKNOWLEDGMENTS

We thank K. Chung, Ravathi, P. Teo, and M. Yeow for technical assistance. This work was supported by research grant MOE2017-T3-1-002 from the Singapore Ministry of Education, opnMe funding from Boehringer-Ingelheim, the Wellcome Trust (award no. 225412/Z/22/Z), and by core funding from the Temasek Life Sciences Laboratory.

AUTHOR CONTRIBUTIONS

M.G. was responsible for experimental work and data analysis; S.S. generated the computational model and network simulations; and M.G. and G.J.A. were responsible for experimental design and manuscript writing.

DECLARATION OF INTERESTS

The authors declare no competing interests.

STAR★METHODS

Detailed methods are provided in the online version of this paper and include the following:

- KEY RESOURCES TABLE
- EXPERIMENTAL MODEL AND STUDY PARTICIPANT DETAILS
 - Animals
 - Stereotaxic injections
- METHOD DETAILS
 - Brain slice recordings
 - Optogenetic characterization of claustral inhibitory circuits
 - Photostimulation of claustral interneurons
 - Design and analysis of optogenetic circuit-mapping experiments
 - Network modeling
- QUANTIFICATION AND STATISTICAL ANALYSIS

SUPPLEMENTAL INFORMATION

Supplemental information can be found online at <https://doi.org/10.1016/j.celrep.2025.116821>.

Received: April 4, 2024

Revised: October 24, 2025

Accepted: December 5, 2025

REFERENCES

- Atlan, G., Matosevich, N., Peretz-Rivlin, N., Yvgi, I., Chen, E., Kleinman, T., Bleistein, N., Sheinbach, E., Groysman, M., Nir, Y., and Citri, A. (2021). Claustral projections to anterior cingulate cortex modulate engagement with the external world. Preprint at bioRxiv. <https://doi.org/10.1101/2021.06.17.448649>.
- Atlan, G., Terem, A., Peretz-Rivlin, N., Sehrawat, K., Gonzales, B.J., Pozner, G., Tasaka, G.I., Goll, Y., Refaeli, R., Zviran, O., et al. (2018). The Claustrum Supports Resilience to Distraction. *Curr. Biol.* 28, 2752–2762.e7. <https://doi.org/10.1016/j.cub.2018.06.068>.
- White, M.G., Mu, C., Qadir, H., Madden, M.B., Zeng, H., and Mathur, B.N. (2020). The Mouse Claustrum Is Required for Optimal Behavioral Performance Under High Cognitive Demand. *Biol. Psychiatry* 88, 719–726. <https://doi.org/10.1016/j.biopsych.2020.03.020>.
- Chevee, M., Finkel, E.A., Kim, S.J., O'Connor, D.H., and Brown, S.P. (2022). Neural activity in the mouse claustrum in a cross-modal sensory selection task. *Neuron* 110, 486–501.e487. <https://doi.org/10.1016/j.neuron.2021.11.013>.
- Liu, J., Wu, R., Johnson, B., Vu, J., Bass, C., and Li, J.X. (2019). The Claustrum-Prefrontal Cortex Pathway Regulates Impulsive-Like Behavior. *J. Neurosci.* 39, 10071–10080. <https://doi.org/10.1523/JNEUROSCI.1005-19.2019>.
- Terem, A., Gonzales, B.J., Peretz-Rivlin, N., Ashwal-Fluss, R., Bleistein, N., Del Mar Reus-Garcia, M., Mukherjee, D., Groysman, M., and Citri, A. (2020). Claustral Neurons Projecting to Frontal Cortex Mediate Contextual Association of Reward. *Curr. Biol.* 30, 3522–3532.e6. <https://doi.org/10.1016/j.cub.2020.06.064>.
- Reus-Garcia, M.M., Sanchez-Campusano, R., Ledderose, J., Dogbevia, G.K., Trevino, M., Hasan, M.T., Gruart, A., and Delgado-Garcia, J.M. (2021). The Claustrum is Involved in Cognitive Processes Related to the Classical Conditioning of Eyelid Responses in Behaving Rabbits. *Cereb. Cortex* 31, 281–300. <https://doi.org/10.1093/cercor/bhaa225>.
- Niu, M., Kasai, A., Tanuma, M., Seiriki, K., Igarashi, H., Kuwaki, T., Nagayasu, K., Miyaji, K., Ueno, H., Tanabe, W., et al. (2022). Claustrum mediates bidirectional and reversible control of stress-induced anxiety responses. *Sci. Adv.* 8, eabi6375. <https://doi.org/10.1126/sciadv.abi6375>.
- Lamsam, L., Liang, M., Gu, B., Sun, G., Hirsch, L.J., Pittenger, C., Kaye, A.P., Krystal, J.H., and Damisah, E.C. (2024). The human claustrum tracks slow waves during sleep. Preprint at bioRxiv. <https://doi.org/10.1101/2024.01.29.577851>.
- Nariykiyo, K., Mizuguchi, R., Ajima, A., Shiozaki, M., Hamanaka, H., Johansen, J.P., Mori, K., and Yoshihara, Y. (2020). The claustrum coordinates cortical slow-wave activity. *Nat. Neurosci.* 23, 741–753. <https://doi.org/10.1038/s41593-020-0625-7>.
- Norimoto, H., Fenk, L.A., Li, H.H., Tosches, M.A., Gallego-Flores, T., Hain, D., Reiter, S., Kobayashi, R., Macias, A., Arends, A., et al. (2020). A claustrum in reptiles and its role in slow-wave sleep. *Nature* 578, 413–418. <https://doi.org/10.1038/s41586-020-1993-6>.
- Renouard, L., Billwiller, F., Ogawa, K., Clément, O., Camargo, N., Abdelkarim, M., Gay, N., Scoté-Blachon, C., Touré, R., Libourel, P.A., et al. (2015). The supramammillary nucleus and the claustrum activate the cortex during REM sleep. *Sci. Adv.* 1, e1400177. <https://doi.org/10.1126/sciadv.1400177>.
- Ntamati, N.R., Acuña, M.A., and Nevian, T. (2023). Pain-induced adaptations in the claustrum-cingulate pathway. *Cell Rep.* 42, 112506. <https://doi.org/10.1016/j.celrep.2023.112506>.
- Wang, Q., Wang, Y., Kuo, H.C., Xie, P., Kuang, X., Hirokawa, K.E., Naeemi, M., Yao, S., Mallory, M., Ouellette, B., et al. (2023). Regional and cell-type-specific afferent and efferent projections of the mouse claustrum. *Cell Rep.* 42, 112118. <https://doi.org/10.1016/j.celrep.2023.112118>.
- Zingg, B., Dong, H.W., Tao, H.W., and Zhang, L.I. (2018). Input-output organization of the mouse claustrum. *J. Comp. Neurol.* 526, 2428–2443. <https://doi.org/10.1002/cne.24502>.
- Shelton, A.M., Oliver, D.K., Lazarte, I.P., Grimstedt, J.S., Kapoor, I., Swann, J.A., Ashcroft, C.A., Williams, S.N., Conway, N., Tir, S., et al. (2022). Single neurons and networks in the claustrum integrate input from widespread cortical sources. Preprint at bioRxiv. <https://doi.org/10.1101/2022.05.06.490864>.
- Atlan, G., Terem, A., Peretz-Rivlin, N., Groysman, M., and Citri, A. (2017). Mapping synaptic cortico-claustral connectivity in the mouse. *J. Comp. Neurol.* 525, 1381–1402. <https://doi.org/10.1002/cne.23997>.
- Chia, Z., Augustine, G.J., and Silberberg, G. (2020). Synaptic Connectivity between the Cortex and Claustrum Is Organized into Functional Modules. *Curr. Biol.* 30, 2777–2790.e4. <https://doi.org/10.1016/j.cub.2020.05.031>.
- Qadir, H., Stewart, B.W., VanRyzin, J.W., Wu, Q., Chen, S., Seminowicz, D.A., and Mathur, B.N. (2022). The mouse claustrum synaptically connects cortical network motifs. *Cell Rep.* 41, 111860. <https://doi.org/10.1016/j.celrep.2022.111860>.
- White, M.G., Panicker, M., Mu, C., Carter, A.M., Roberts, B.M., Dharmasri, P.A., and Mathur, B.N. (2018). Anterior Cingulate Cortex Input to the Claustrum Is Required for Top-Down Action Control. *Cell Rep.* 22, 84–95. <https://doi.org/10.1016/j.celrep.2017.12.023>.
- Kepecs, A., and Fishell, G. (2014). Interneuron cell types are fit to function. *Nature* 505, 318–326. <https://doi.org/10.1038/nature12983>.
- Markram, H., Toledo-Rodriguez, M., Wang, Y., Gupta, A., Silberberg, G., and Wu, C. (2004). Interneurons of the neocortical inhibitory system. *Nat. Rev. Neurosci.* 5, 793–807. <https://doi.org/10.1038/nrn1519>.
- Kim, J., Lee, S., Tsuda, S., Zhang, X., Asrican, B., Gloss, B., Feng, G., and Augustine, G.J. (2014). Optogenetic mapping of cerebellar inhibitory circuitry reveals spatially biased coordination of interneurons via electrical synapses. *Cell Rep.* 7, 1601–1613. <https://doi.org/10.1016/j.celrep.2014.04.047>.
- Petreanu, L., Huber, D., Sobczyk, A., and Svoboda, K. (2007). Channelrhodopsin-2-assisted circuit mapping of long-range callosal projections. *Nat. Neurosci.* 10, 663–668. <https://doi.org/10.1038/nn1891>.
- Wang, H., Peca, J., Matsuzaki, M., Matsuzaki, K., Noguchi, J., Qiu, L., Wang, D., Zhang, F., Boyden, E., Deisseroth, K., et al. (2007). High-speed mapping of synaptic connectivity using photostimulation in Channelrhodopsin-2 transgenic mice. *Proc. Natl. Acad. Sci. USA* 104, 8143–8148. <https://doi.org/10.1073/pnas.0700384104>.
- Graf, M., Nair, A., Wong, K.L.L., Tang, Y., and Augustine, G.J. (2020). Identification of Mouse Claustral Neuron Types Based on Their Intrinsic Electrical Properties. *eNeuro* 7, ENEURO.0216-20.2020. <https://doi.org/10.1523/ENEURO.0216-20.2020>.
- Stevens, C.F. (1976). A comment on Martin's relation. *Biophys. J.* 16, 891–895. [https://doi.org/10.1016/S0006-3495\(76\)85739-6](https://doi.org/10.1016/S0006-3495(76)85739-6).
- Lee, A.J., Wang, G., Jiang, X., Johnson, S.M., Hoang, E.T., Lanté, F., Stornetta, R.L., Beenhakker, M.P., Shen, Y., and Julius Zhu, J. (2015). Canonical Organization of Layer 1 Neuron-Led Cortical Inhibitory and Disinhibitory Interneuronal Circuits. *Cereb. Cortex* 25, 2114–2126. <https://doi.org/10.1093/cercor/bhu020>.
- Pfeffer, C.K., Xue, M., He, M., Huang, Z.J., and Scanziani, M. (2013). Inhibition of inhibition in visual cortex: the logic of connections between molecularly distinct interneurons. *Nat. Neurosci.* 16, 1068–1076. <https://doi.org/10.1038/nn.3446>.

30. Pi, H.J., Hangya, B., Kvitsiani, D., Sanders, J.I., Huang, Z.J., and Kepecs, A. (2013). Cortical interneurons that specialize in disinhibitory control. *Nature* 503, 521–524. <https://doi.org/10.1038/nature12676>.
31. Real, M.A., Dávila, J.C., and Guirado, S. (2003). Expression of calcium-binding proteins in the mouse claustrum. *J. Chem. Neuroanat.* 25, 151–160. [https://doi.org/10.1016/s0891-0618\(02\)00104-7](https://doi.org/10.1016/s0891-0618(02)00104-7).
32. Ferguson, K.A., and Cardin, J.A. (2020). Mechanisms underlying gain modulation in the cortex. *Nat. Rev. Neurosci.* 21, 80–92. <https://doi.org/10.1038/s41583-019-0253-y>.
33. Silver, R.A. (2010). Neuronal arithmetic. *Nat. Rev. Neurosci.* 11, 474–489. <https://doi.org/10.1038/nrn2864>.
34. Ollerenshaw, D.R., Davis, J., McBride, E.G., Shelton, A., Koch, C., and Olsen, S.R. (2021). Anterior claustrum cells are responsive during behavior but not passive sensory stimulation. Preprint at bioRxiv. <https://doi.org/10.1101/2021.03.23.436687>.
35. Marriott, B.A., Do, A.D., Zahacy, R., and Jackson, J. (2021). Topographic gradients define the projection patterns of the claustrum core and shell in mice. *J. Comp. Neurol.* 529, 1607–1627. <https://doi.org/10.1002/cne.25043>.
36. Chia, Z., Silberberg, G., and Augustine, G.J. (2017). Functional properties, topological organization and sexual dimorphism of claustrum neurons projecting to anterior cingulate cortex. *Clastrum* 2, 1357412. <https://doi.org/10.1080/20023294.2017.1357412>.
37. Erwin, S.R., Bristow, B.N., Sullivan, K.E., Kendrick, R.M., Marriott, B., Wang, L., Clements, J., Lemire, A.L., Jackson, J., and Cembrowski, M.S. (2021). Spatially patterned excitatory neuron subtypes and projections of the claustrum. *eLife* 10, e68967. <https://doi.org/10.7554/eLife.68967>.
38. White, M.G., and Mathur, B.N. (2018). Claustrum circuit components for top-down input processing and cortical broadcast. *Brain Struct. Funct.* 223, 3945–3958. <https://doi.org/10.1007/s00429-018-1731-0>.
39. Kim, J., Matney, C.J., Roth, R.H., and Brown, S.P. (2016). Synaptic Organization of the Neuronal Circuits of the Claustrum. *J. Neurosci.* 36, 773–784. <https://doi.org/10.1523/JNEUROSCI.3643-15.2016>.
40. Nair, A., Teo, Y.Y., Augustine, G.J., and Graf, M. (2023). A functional logic for neurotransmitter corelease in the cholinergic forebrain pathway. *Proc. Natl. Acad. Sci. USA* 120, e2218830120. <https://doi.org/10.1073/pnas.2218830120>.
41. Karnani, M.M., Agetsuma, M., and Yuste, R. (2014). A blanket of inhibition: functional inferences from dense inhibitory connectivity. *Curr. Opin. Neurobiol.* 26, 96–102. <https://doi.org/10.1016/j.conb.2013.12.015>.
42. Fodoulian, L., Gschwend, O., Huber, C., Mutel, S., Salazar, R.F., Leone, R., Renfer, J.-R., Ekundayo, K., Rodriguez, I., and Carleton, A. (2020). The claustrum-medial prefrontal cortex network controls attentional set-shifting. Preprint at bioRxiv. <https://doi.org/10.1101/2020.10.14.339259>.
43. Demsar, J., Curk, T., Erjavec, A., Gorup, C., Hocevar, T., Milutinovic, M., Mozina, M., Polajnar, M., Toplak, M., Staric, A., et al. (2013). Orange: data mining toolbox in python. *J. Mach. Learn. Res.* 14, 2349–2353.
44. Schindelin, J., Arganda-Carreras, I., Frise, E., Kaynig, V., Longair, M., Pietzsch, T., Preibisch, S., Rueden, C., Saalfeld, S., Schmid, B., et al. (2012). Fiji: an open-source platform for biological-image analysis. *Nat. Methods* 9, 676–682. <https://doi.org/10.1038/nmeth.2019>.

STAR★METHODS

KEY RESOURCES TABLE

REAGENT or RESOURCE	SOURCE	IDENTIFIER
Bacterial and virus strains		
pAAV-CaMKIIa-hChR2(H134R)-EYFP	Addgene	26969-AAV1
pAAV-mDlx-NLS-mRuby2	Addgene	99130-AAV1
Chemicals, peptides, and recombinant proteins		
Alexa-dye 596	Thermo Fisher Scientific	A10438
Adenosine-5'-triphosphate Di-sodium hydrate	Sigma-Aldrich	A7699
Ascorbic acid	Nacalai Tesque	03420-52
Calcium chloride	Sigma-Aldrich	C1016
Disodium phosphocreatinine	Sigma-Aldrich	P7936
EGTA	Sigma-Aldrich	E3889
GABAzine	Tocris Bioscience	1262
Glucose	Sigma-Aldrich	616338
Guanosine 5'-triphosphate sodium salt hydrate	Sigma-Aldrich	G8877
HEPES	Sigma-Aldrich	H3375
Isoflurane	Chemical Iberica	26675-46-7
Kynurenic acid	Sigma-Aldrich	K3375
Magnesium chloride	Sigma-Aldrich	M8266
Mineral oil	Sigma-Aldrich	M5904
Monosodium phosphate dihydrate	Sigma-Aldrich	71505
Myo-inositol	Sigma-Aldrich	I5125
Potassium chloride	Sigma-Aldrich	P9541
Potassium gluconate	Sigma-Aldrich	P1847
Potassium hydroxide	Kanto Chemical	3234400
Sodium bicarbonate	Nacalai Tesque	31213-15
Sodium chloride	Sigma-Aldrich	S7653
Sodium pyruvate	Sigma-Aldrich	P2256
Sucrose	Sigma-Aldrich	S7903
Experimental models: Organisms/strains		
parvalbumin-cre mice (B6;129P2- <i>Pvalb</i> ^{tm1(cre)Arbr/J})	Jackson Laboratory	008069
somatostatin-cre mice (B6;129S4- <i>Sst</i> ^{tm2.1(cre)Zjh/J})	Jackson Laboratory	013044
vasoactive-intestinal-peptide-cre mice (B6;129S4- <i>Vip</i> ^{tm1(cre)Zjh/J})	Jackson Laboratory	010908
loxP-STOP-loxP-channelrhodopsin2-eYFP mice (B6;129S-Gt(<i>ROSA</i>)26Sor ^{tm32(CAG-COP4*H134R/EYFP)Hze/J})	Jackson Laboratory	012569
Software and algorithms		
Clampfit 10.2	Molecular devices	RRID:SCR_011323
Fiji/ImageJ	NIH	RRID:SCR_003070
MATLAB R2015	Mathworks	RRID:SCR_001622
Orange Data Mining	Demsar et al. ⁴³ ; see Schindelin et al. ⁴⁴	https://orange.biolab.si/
Origin	Origin Lab	RRID:SCR_014212
SPSS	IBM	RRID:SCR_002865

EXPERIMENTAL MODEL AND STUDY PARTICIPANT DETAILS

Animals

All animal experiments were approved by the Institutional Animal Care and Use Committees of Nanyang Technological University and Temasek Life Sciences Laboratory, Singapore. We used transgenic mice of both sexes from the following lines: parvalbumin-cre

(B6;129P2-*Pvalb*^{tm1(cre)Arbr}/J; Jackson Laboratory: #008069), somatostatin-cre (B6;129S4-*Sst*^{tm2.1(cre)Zjh}/J; Jackson Laboratory: #013044), vasoactive-intestinal-peptide-cre (B6;129S4-*Vip*^{tm1(cre)Zjh}/J; Jackson Laboratory: #010908). These were mated with loxP-STOP-loxP-channelrhodopsin2-eYFP mice (B6;129S-*Gt(ROSA)26Sor*^{tm32(CAG-COP4*H134R/EYFP)Hze}/J; Jackson Laboratory: #012569) to produce heterozygous mice expressing one allele of the H134R variant of channelrhodopsin-2 exclusively in PV-INs, SST-INs or VIP-INs. The average age of mice used in our experiments was postnatal day 65.5 ± 0.6 days.

Stereotaxic injections

For the experiments of Figure 7, viruses were injected into the brain to express ChR2 in ACC projection neurons and a fluorescent protein (mRuby) in claustral INs. To inject these viruses, mice were anesthetized with isoflurane and placed in a stereotaxic frame (Harvard Apparatus). An incision was made along the scalp to access the bregma and the injection site. Craniotomy surgery and viral injections were performed at the following locations. To express ChR2 in prefrontal projection neurons: AP: −1 mm from bregma, ML: 0.25 mm, DV: −1.4 mm. To label claustral INs: AP: −1 mm, ML: 2.7 mm, DV: 2.7 mm. Pulled glass pipettes were back-filled with mineral oil and 200 nL of undiluted AAV virus. For PN AAV-CamK2a-ChR2, Addgene: 26969; Titer: 1 × 10¹³ vg/mL was used. For claustral INs AAV-Dlx5/6-mRuby, Addgene: 99130; Titer: 1 × 10¹³ vg/mL was used. The glass pipettes were lowered to the injection location and AAV virus was pressure injected at 10 nL/s for 1 s and then at a rate of 2 nL/s for the remaining volume. To minimize leakage during withdrawal, the pipette was held in place for 5 min before being slowly retracted from the brain.

METHOD DETAILS

Brain slice recordings

Acute brain slices were prepared according to the procedures described in Graf et al.²⁶ Mice were deeply anesthetized with isoflurane and euthanized via decapitation. The brains were isolated and transferred into ice-cold sucrose solution containing (in mM): sucrose 250, NaHCO₃ 26, glucose 10, MgCl₂ 4, myo-inositol 3, KCl 2.5, sodium pyruvate 2, NaH₂PO₄ 1.25, ascorbic acid 0.5, CaCl₂ 0.1, kynurenic acid 1, with an osmolality of 350–360 mOsm and a pH of 7.4. Coronal brain slices (250 μm thickness) were cut with a Leica VT 1000S vibratome. Slices were kept for 0.5 h at 34°C in artificial cerebrospinal fluid (ACSF) containing (in mM): NaCl 126, NaHCO₃ 24, NaH₂PO₄ 1, KCl 2.5, CaCl₂ 2, MgCl₂ 2, glucose 10, ascorbic acid 0.4, 300–310 mOsm, pH 7.4) and gassed with a 95% O₂/5% CO₂ mixture before transfer to ACSF at room temperature for recordings.

The claustrum was identified in brain slices via anatomical landmarks (distance to external capsule, inflection point of external capsule) and the IN-specific expression of ChR2-eGFP, as previously described.²⁶ Whole-cell patch recordings were performed with borosilicate glass pipettes (5–9 MΩ) filled with internal solution containing (in mM): K-gluconate 130, KOH 10, MgCl₂ 2.5, HEPES 10, Na₂ATP 4, Na₃GTP 0.4, EGTA 5, Na₂ phosphocreatinin 5 and Alexa-dye 596 (290–295 mOsm, pH 7.4). All recordings were performed at 24°C with a Multiclamp 700B amplifier (Molecular Devices) and a Digidata 1440 interface (Molecular Devices). Signals were acquired at 50 kHz and filtered at 10 kHz. Electrical signals were analyzed with a variety of software: Clampfit 10.2 (Molecular Devices), Origin (OriginLab), Excel (Microsoft), Orange3⁴³ and custom-written MATLAB (Mathworks, R2015). Images of neurons filled with Alexa dye were acquired on an Olympus FV1000MPE2 2-photon microscope; image analysis and processing were done with Fiji/ImageJ software.⁴⁴

Optogenetic characterization of claustral inhibitory circuits

The connectivity of claustral INs was probed by photostimulating ChR2-expressing presynaptic INs while measuring electrical responses in postsynaptic neurons. For presynaptic neurons, ChR2 was specifically expressed in PV-INs, SST-INs or VIP-INs using the transgenic strategy described above. Postsynaptic INs were classified into the 8 subtypes identified in a previous classification scheme²⁶ that is based on 63 intrinsic electrical properties, including adaptation of AP amplitude, as well as the amplitudes of AP afterdepolarizations and afterhyperpolarizations. This yielded clear differences between PN1 projection neurons, PN2–PN5 projection neurons, and PV-INs, SST-INs and VIP-INs (Figure S1A). The circuit properties of all 8 subtypes of postsynaptic neurons are illustrated in the supplemental information (Figures S3–S8). In the interest of clarity, we also employed a simplified scheme that classified claustrum neuron subtypes according to PN anatomical projection patterns and expression of IN markers (Figure S1B). In this simplified scheme, PN1 were classified as claustrum-subcortical projecting neurons (CS-PNs; Figure S1B, cyan) and were characterized by their strong AP amplitude adaptation (Figure S1C). PN2–PN5 neurons were grouped as claustrum-cortical projection neurons (CC-PNs; Figure S1B, violet) that could be identified by their strong-AP frequency adaptation (Figure S1D). Although PV-INs, SST-INs, and VIP-INs were pooled into a single IN group (Figures S1B and S1E), our computational models utilized the characteristic connectivity properties of each subtype of IN. Postsynaptic cells that expressed ChR2 were not included to characterize the local connectivity. Because the penetrance of ChR2 expression was not 100% in any of the transgenic lines, it was also possible to characterize PV-IN-to-PV-IN, SST-IN-to-SST-IN, and VIP-IN-to-VIP-IN connections in a subset of experiments where the postsynaptic INs did not express channelrhodopsin. This strategy allowed us to measure IPSCs without contamination by photocurrents.

Photostimulation of claustral interneurons

Two different strategies were employed to photostimulate INs in brain slices from transgenic mice. The procedures used for each are described here and statistical analyses of the resultant data are summarized in Table S1.

Wide-field illumination

To measure maximum inhibitory effects, the entire field of view was illuminated over an area of $0.24 \mu\text{m}^2$ (Figure 1A) using a band-pass-filtered mercury arc lamp ($14.6 \text{ mW}/\text{mm}^2$ irradiance at 480 nm). Postsynaptic responses to light flashes were averaged 3–10 times and signals were considered IPSCs if their peak amplitude was at least 3 standard deviations above the baseline noise. We used two light stimulus durations: a 1.2 ms light flash to quantify input amplitude while minimizing the triggering of multiple presynaptic action potentials and a 500 ms flash, which increased the likelihood of evoking an IPSC from all INs. Response rates (Figure 1I) were calculated based on the 500 ms stimulus, while response amplitudes (Figure 1H) were determined from the 1.2 ms stimulus. VIP-IN-to-CS-PN connections were an exception: the amplitudes of these IPSCs were only reliably measurable in response to 500 ms flashes.

Focal laser illumination

For measuring spatially resolved circuit mapping, the microscope field ($508 \times 508 \mu\text{m}^2$) was divided into a 32×32 pixel array (1024 pixels, each $252 \mu\text{m}^2$). All pixels within this array were illuminated by a focal laser spot (488 nm, 4 ms duration, approximately $1 \mu\text{m}$ diameter in the focal plane) that was pseudorandomly scanned to avoid use-dependent effects, such as short-term synaptic plasticity. This mode of photostimulation allowed quantification of spatially-resolved inputs from individual presynaptic INs. To calculate the unitary IPSC amplitude for a distinct IN-postsynaptic neuron connection, all IPSCs were pooled and modal IPSC amplitude was determined as the peak of the IPSC amplitude distribution.

Design and analysis of optogenetic circuit-mapping experiments

This section describes how local IN circuits were spatially mapped via focal laser photostimulation.

Optical footprint determination

For each IN subtype, laser power was optimized to be high enough to evoke APs in every channelrhodopsin-expressing IN, but low enough so that APs were evoked only when the laser light spot was located over the soma or proximal dendrites of the IN. To identify the optimal light power for such optogenetic control of claustral INs, ChR2-expressing claustral INs were whole-cell patch clamped (Figure S4A) and then illuminated by the small laser light spot. Diffusion of Alexa 594 dye within the internal solution of the patch pipette into the IN visualized IN morphology and enabled correlation of the IN light-evoked response with its morphology (Figure S4B). Optimal photostimulation evoked AP firing only in the soma and proximal dendrites of the patched neuron (Figure S4B) but not in distal dendrites, axons or the surrounding area. The minimum laser power required to reliably evoke somatic AP firing differed for each subtype of ChR2-expressing IN and was $56 \mu\text{W}$ for PV-INs (Figure S5A, arrow), $62 \mu\text{W}$ for SST-INs (Figure S5B, arrow) and $70 \mu\text{W}$ for VIP-INs (Figure S5C).

The optical footprint of ChR2 expressing presynaptic INs was defined as the area over which laser spots were capable of evoking APs (red pixels in Figure S4B). In all IN lines, the optical footprint had a bimodal distribution (Figures S5D–S5F), presumably reflecting heterogeneity in ChR2 expression levels and/or neuronal morphology. To estimate average optical footprint area, the weighted median was calculated based on the relative percentage of neurons with small or large optical footprint and their respective median footprint areas (Figures S5D–S5F):

$$\text{WeightedmedianIN} = (p_s \times M_s) + (p_L \times M_L), \quad (\text{Equation 1})$$

where p_s is the probability of small optical footprints, p_L is the probability of large optical footprints, M_s is the median area of small optical footprints and M_L is the median area of large optical footprints. The weighted median of the optical footprint area for PV-INs was $2544 \mu\text{m}^2$ (Figures S4C and S5D), $5656 \mu\text{m}^2$ for SST-INs (Figures S4C and S5E) and $13069 \mu\text{m}^2$ for VIP-INs (Figures S4C and S5F).

To determine when photostimulation evoked APs in INs, we measured the latency between stimulus onset and the time of AP peak. The median latency between the onset of the light stimulus and the light-evoked AP was 8.0 ms in PV-INs, 9.6 ms for SST-INs and 12.4 ms in VIP-INs (Figures S5G–S5I). A small fraction of APs in SST-INs and VIP-INs were evoked between 20 and 25 ms (SST-IN: 45/1205 APs; VIP-IN: 404/4524 APs). Thus, IPSCs in postsynaptic neurons were considered to be evoked by photostimulation of presynaptic INs only if they occurred within 25 ms after stimulus onset.

Input mapping

To map the spatial organization of claustral inhibitory circuitry, INs were focally stimulated (with optimized laser power) over the array of 1024 laser spot locations and light-evoked IPSCs were measured in postsynaptic neurons held at a membrane potential of -40 mV . If the laser spot evoked a light-evoked IPSC, then the location of the spot indicated the presence of the somata or proximal dendrites of a presynaptic IN (Figures 2A and S4D–S4F). Criteria used to identify light-evoked IPSCs were: (a) latency within 25 ms after stimulus onset; (b) peak amplitude at least 4 times larger than the standard deviation of the baseline noise; (c) duration longer than 0.6 ms at the detection threshold; and (d) present in a majority of trials (3–5 trials per location). Locations where IPSCs fulfilled these criteria were binarized to identify positions of inhibitory inputs (Figure S4F). The combined area of these locations represented the input field resulting from all presynaptic INs (Figure 2A).

Input probability mapping

Because laser power was optimized to evoke APs only when laser spots were positioned over IN somata and proximal dendrites, the positions that evoked postsynaptic IPSCs revealed the location of presynaptic INs. Thus, by calculating a location-specific input distribution, it was possible to calculate connection probabilities that mirrored the connectivity between presynaptic INs and their target

neurons. To calculate the average probability distribution map, all binarized input maps were rotated until the external capsule was aligned dorsal-to-ventrally and on the left side of the input field, while the location of the patched cell was kept constant at the center of the input map. Next, all input maps from the same IN-to-postsynaptic neuron connection were combined and the location-specific input probability relative to the location of the postsynaptic neuron was calculated as:

$$\text{Input probability}_{px} = \left(\frac{\sum \text{binary value at } px \text{ across all binary maps}}{\text{total number of binary maps}} \right), \quad (\text{Equation 2})$$

where px = pixel position within a 32×32 grid (1024 pixels). To quantify differences in the spatial distribution of input probabilities, average input distributions were binned (bin width 100 μm) along the central dorsoventral (DV) or medio-lateral (ML) axis, resulting in connection-specific DL and ML input profiles. Input profiles were fitted and differences in input profiles were quantified using the full-width at half-maximum (FWHM) distances of the fitted input profiles.

IN convergence calculation

To estimate the number of presynaptic INs that converged onto the same postsynaptic target neuron, we calculated the ratio of population mean of input area and optical footprint area:

$$\text{IN convergence} = \text{mean} \frac{\text{population mean of Input area}}{\text{weighted median optical footprint}}. \quad (\text{Equation 3})$$

Network modeling

To simulate claustral network activity, a network of N neurons composed of N_E excitatory and N_I inhibitory units ($N = N_E + N_I$) was generated. The inhibitory network consisted of subpopulations of PV-INs, SST-INs and VIP-INs ($N_I = N_{PV} + N_{SST} + N_{VIP}$). The dynamics of neuronal activity was simulated by solving the following N-dimensional differential equations:

$$\tau \frac{dr}{dt} = -r + \Phi(Wr + I), \quad (\text{Equation 4})$$

which describe changes in the average firing rate of neurons as a function of external and recurrent inputs to them. Here, r is a $1 \times N$ vector of firing rates composed of the activity of different subpopulations: $r_E, r_{PV}, r_{SST}, r_{VIP}$ ($r = [r_E, r_{PV}, r_{SST}, r_{VIP}]$). τ is the time constant of the network integration, and $\Phi(x)$ denotes the activation function, which is assumed to be a linear rectified function:

$$\Phi(x) = 0, \text{ if } x < 0; \Phi(x) = x, \text{ if } x > 0, \quad (\text{Equation 5})$$

where I denotes the $1 \times N$ vector of external input to neurons, and W is the $N \times N$ weight matrix of the network describing the connection weights between all pairs of excitatory and inhibitory neurons. We describe how the external input and the weight matrix are obtained as a function of spatial position of neurons in the following.

Spatial network

To model the distance dependent connectivity of inhibitory connections, the network models were simulated with spatial profiles. Neurons are located on a ring with the size of $L = 1\text{mm}$. To avoid boundary effects, the locations were wrapped around on a torus (i.e., $x = L$ is the same as $x = 0$). Neurons belonging to each subpopulation tile the space with equal distances, respectively. For instance, excitatory neurons with ID's $[1, 2, \dots, N_E]$ are allocated the spatial positions of $x_E = [0, L/N_E, \dots, L(N_E - 1)/N_E]$. Similarly, the positions of PV-IN, SST-IN, and VIP-INs are given, respectively, by: $x_{PV} = [0, L/N_{PV}, \dots, L(N_{PV} - 1)/N_{PV}]$, $x_{SST} = [0, L/N_{SST}, \dots, L(N_{SST} - 1)/N_{SST}]$, and $x_{VIP} = [0, L/N_{VIP}, \dots, L(N_{VIP} - 1)/N_{VIP}]$.

Weight matrix

The matrix of connection weights, W , in spatial networks was obtained as a function of the spatial distances between pairs of neurons. For a pair of neurons with positions x_i and x_j , the weight of the connection, w_{ij} , was given by:

$$w_{ij} = \alpha_{ij} \exp(-d_{ij}/\sigma_{ij}), \quad (\text{Equation 6})$$

where d_{ij} is the distance between the pair of neurons. The distance was obtained as $d_{ij} = |x_i - x_j|$, where $|\cdot|$ denotes the absolute value. To impose the wrapped around boundary condition, we have: $d_{ij} = L - |x_i - x_j|$, if $|x_i - x_j| > L/2$. α determines the strength, and σ sets the spatial extent of connectivity. They were set differently depending on the pre-synaptic and post-synaptic subpopulations from which a pair of neurons were selected. These values were specified by the following matrices.

Matrix S describes the spatial extent of connectivity between all pairs of subpopulations. It is a 4×4 matrix with the n -th row and m -th column entry specifying the spatial constant of connectivity between the n -th presynaptic ($X \in \{E, PV, SST, VIP\}$) and the m -th postsynaptic subpopulation ($Y \in \{E, PV, SST, VIP\}$): $S(n, m) = \sigma_{X \rightarrow Y}$. The values were obtained from the best exponential fits to the respective empirically measured distributions.

The strength of connectivity, α , was determined by the 4×4 matrix A . Its n -th row and m -th column entry specify the average strength of the total input a neuron in the m -th post-synaptic subpopulation receives from the n -th pre-synaptic subpopulation: $A(n, m) = \alpha_{X \rightarrow Y}$. The values were either obtained from the empirically measured wide-field inputs (global connectivity strength) or were derived as the product of local IN convergence with modal IPSC amplitude (local connectivity strength).

Knowing matrices A and S , the weight of connections between pairs of neurons from the given presynaptic and postsynaptic subpopulations ($\{X \rightarrow Y\}$) were obtained as the following. The initial weight was calculated from the respective pairwise distances for all neurons in subpopulations X and Y (Eq. vi). The $N_X \times N_Y$ sub-matrix of connectivity was then normalized such that the average (over neurons in the post-synaptic subpopulation, Y) of the total weight (from the pre-synaptic subpopulation, X) is equal to $\alpha_{X \rightarrow Y}$. Finally, the entries of the weight matrix were multiplied by a random value drawn from a uniform distribution between $[0, 1]$, to account for randomness in connectivity.

External input

The external inputs to neurons consisted of a tuned component, I_s , which was a function of the stimulus location and the location of the neuron. The stimulus-specific, tuned component of the input was given by a von Mises function:

$$I_s = \left(s_b + s_m \exp\left(\alpha \cos\left(\frac{2\pi}{L}(x_i - x_s)\right)\right) \right) / \exp(\alpha) * (r_l + \text{rand}() * r_u), \quad (\text{Equation 7})$$

where s_b is the baseline input and s_m is the modulation component. x_i is the location of neuron i , and x_s is the location of the stimulus. α controls the sharpness of tuning in the von Mises function. We assume $x_s = L/2$ and $L = 1$. $\alpha = 0$ for a uniform excitatory input, $\alpha = 2$ for the more spatially tuned excitatory inputs. To model noisy inputs, the location-specific inputs were multiplied by a randomly drawn number between 0 and 2 ($r_l = 0$, $r_u = 2$) and were set to $r_l = 1$ and $r_u = 0$ for noise-free simulations.

Default parameters

Unless otherwise stated, the following parameters were used for simulations.

Number of neurons: $N_E = 500$, $N_{PV} = 100$, $N_{SST} = 100$, $N_{VIP} = 100$.

Temporal parameters: $\tau = 10$, $dt = 1$, and total time of simulation $T = 1000$.

Input parameters: $bb = \{0, 0, 0, 0\}$ and $mm = \{2, 4, 4, 4\}$ for neurons belonging to the respective populations, $\{E, PV, SST, VIP\}$. External inputs to INs were chosen to be 2 times larger than PN inputs, based on the empirically measured larger external inputs onto claustral PV-INs when compared to PNs.^{18,39}

Spatial connectivity parameters for CS-PNs or CC-PNs:

$$S_{CS} = \begin{pmatrix} 0.15 & 0.15 & 0.15 & 0.15 \\ 0.13 & 0.15 & 0.14 & 0.22 \\ 0.21 & 0.17 & 0.33 & 0.2 \\ 0.19 & 0.14 & 0.21 & 0.27 \end{pmatrix}; S_{CC} = \begin{pmatrix} 0.15 & 0.15 & 0.15 & 0.15 \\ 0.17 & 0.15 & 0.14 & 0.2 \\ 0.24 & 0.17 & 0.33 & 0.2 \\ 0.18 & 0.14 & 0.21 & 0.27 \end{pmatrix}.$$

Asymmetry matrix to include medio-lateral inhibition differences:

$$d_{oCS} = \begin{pmatrix} 0 & 0 & 0 & 0 \\ 0.001 & 0.032 & -0.005 & 0.026 \\ 0.037 & 0.024 & 0.079 & 0.038 \\ 0.013 & -0.033 & 0.015 & 0.068 \end{pmatrix},$$

$$d_{oCC} = \begin{pmatrix} 0 & 0 & 0 & 0 \\ 0.007 & 0.032 & -0.005 & 0.026 \\ 0.012 & 0.024 & 0.079 & 0.038 \\ 0.019 & -0.033 & 0.015 & 0.068 \end{pmatrix}.$$

Local connectivity strength:

$$A_{CSlocal} = \begin{pmatrix} 0.1 & 0.33 & 0.33 & 0.33 \\ -0.09 & -0.31 & -0.14 & -0.02 \\ -0.25 & -0.25 & -0.24 & -0.02 \\ -0.03 & -0.07 & -0.03 & -0.004 \end{pmatrix}; A_{CClocal} = \begin{pmatrix} 0.1 & 0.33 & 0.33 & 0.33 \\ -0.32 & -0.31 & -0.14 & -0.02 \\ -0.40 & -0.25 & -0.24 & -0.02 \\ -0.01 & -0.07 & -0.03 & -0.004 \end{pmatrix}.$$

Global connectivity strength:

$$A_{CSglobal} = \begin{pmatrix} 0.1 & 0.33 & 0.33 & 0.33 \\ -0.3 & -0.57 & -0.28 & -0.08 \\ -0.56 & -0.35 & -0.29 & -0.37 \\ -0.04 & -0.13 & -0.15 & -0.06 \end{pmatrix}; A_{CCglobal} = \begin{pmatrix} 0.1 & 0.33 & 0.33 & 0.33 \\ -1 & -0.57 & -0.28 & -0.08 \\ -0.9 & -0.35 & -0.29 & -0.37 \\ -0.05 & -0.13 & -0.15 & -0.06 \end{pmatrix}.$$

To assess the specific effect of each inhibitory connection on the total activity of E neurons, we ran the model with two weight matrices. First, the activity of E neurons (r_0) is obtained by using the original weight matrix (W_0). We then deactivated the specific inhibitory connections and ran the model with the next weight matrix (W_1), to obtain the new activity of E neurons (r_1). The difference in the activity, $dr = r_1 - r_0$, was calculated and used as the effect of the specific connection that was deactivated.

QUANTIFICATION AND STATISTICAL ANALYSIS

To test for normal distribution of experimental results, a Shapiro-Wilk test was performed. The medians of non-normal distributed experimental data were compared by using a Kruskal-Wallis test. To test for significant differences in between groups, a Dunn's post hoc comparison with Bonferroni adjustment was performed.